O. Jaïbi

Topology and geometry in a quantum condensed matter system: Weyl semimetals.

Master Thesis

Supervisors:

Dr. R-J. Slager

Prof. Dr. J. Zaanen

Institute Lorentz, Leiden University

Abstract

Weyl semimetals have been providing for a considerable research interest in the last decade in quantum condensed matter physics, due to their non-trivial topological nature and their possible applications in material science. Their non-trivial topological order has many consequences like zero energy Weyl nodes, which are robust to impurities and display a chiral anomaly. The work presented in this thesis is inspired by the intriguing matter of the response of Weyl semimetals to topological defects and their change to the behaviour of underlying lattice. To achieve this, we studied the response of different types of Weyl semimetals upon introducing a lattice dislocation or a π-flux vortex, which mimics the effect of the former. Specifically, we show that the existence of a (or multiple) Kramers pair(s) of zero-energy modes bound to a dislocation line or vortex is a not a generic feature of topologically non-trivial phases of Weyl semimetals since this appears to depend on the present number of Weyl nodes and their chiralities as well as the type of symmetry breaking. We obtain the explicit form of these states, which shows their exponentially localised nature. Furthermore, we analyse the dependence of the energy of these dislocation modes on different parameters of the models and analyse the resulting correlations found. We then conclude by placing these results in a broader context.

Contents

Chapter 1

Introduction

This chapter addresses the fundamental aspects of topologically ordered condensed matter systems. Starting from some general notions, the theoretical and experimental advances related to the topological band insulator are discussed from a historical perspective. The chapter goes on with topological (semi-)metals, focused on Weyl semimetals and concludes with an overview of this thesis.

Condensed matter physics starts at microscopic scales with a clear notion of space-time distance [1]. However, it has been understood since the discovery of the integer quantum Hall effect that some phases of matter, known as topological phases, reflect the emergence of a different type of behaviour that "seems" independent of space-time, where the macroscopic physics is governed by properties that are described by the branch of mathematics known as topology. The emergence of a topological description reflects a type of order in condensed matter physics that is quite different from conventional spin-split Fermi orders, described in

terms of symmetry breaking.

Since the discovery of topological band insulators, interest in these type of materials has steadily grown. A closely related state of matter, known as a Weyl semimetal, is of great interest, since it unveils Fermi arc surface states as well as a chiral anomaly and theoretically represents the surface state of four dimensional Chern insulators. The possible experimental realisations with real material candidates make this phase of matter even more interesting for its potential applications.

1.1 Topology

Topology is a branch of mathematics that can be used to describe properties of classes of objects that are invariant under continuous smooth transformations, known as homotopies. The most commonly used example is the topological equivalence between a coffee mug and a torus, since one can be continuously transformed into another (without closing or opening any holes) as can be seen in Figure 1.1.

Another example would be the topology of knots, where two knots

Figure 1.1: Deformation from coffee mug into a donut. Taken from [2].

on a closed loop are equivalent if they can be transformed into another without cutting a string. A knot in a manifold M is a submanifold of M that is diffeomorphic to a circle. A link is a submanifold diffeomorphic to a disjoint union of circles. Knots and links are typically represented by drawing two dimensional diagrams [3]. In order to describe such structures, topological invariants are defined, being the analogue of the

order parameters associated with broken symmetries.

Following this analogy, the topological classification of general gapped many-body states of matter may be used to describe the subclass of states that can be described by the band theory of solids. The shape of the band structure and how the energy bands are knotted defines topological invariants characterizing different equivalence classes of knotted spectra, that can continuously be deformed into each other. This allows for the notion of topological equivalence classes based on the principle of adiabatic continuity. A quantum state may be called topological when its wavefunctions bear a distinct character that can be specified by some topological invariant, a discrete quantity that remains unchanged upon adiabatic deformations of the system. Materials realising such topological order are called topological materials. To put this in perspective, consider a normal insulator, being characterised by an energy gap E_G. Insulators are topologically equivalent if they can be changed into one another by slowly changing the Hamiltonian, such that the system always remains in its ground state and thus preserving the finite band gap E_G. This means that the topology of bands of an insulator is protected and that connecting topologically inequivalent insulators necessarily involves a gap closure in which the energy gap vanishes, which boils down to connecting two topologically different vacua. Since topological insulators display a metallic surface state, they can thus be distinguished from the ordinary ones by means of topology. This is essentially the definition of a topological insulator.

1.2 Historical perspective

In the 1980's the discovery of the integer quantum Hall effect [4, 5] gave rise to new perspectives in the study of quantum condensed matter. Consider the quantum Hall state, where electrons are confined to a two-dimensional plane and exposed to a strong magnetic field perpendicular to their motion. The electrons then circulate in quantised orbits with quantised levels of energy i.e. Landau levels. Along with the topological nature of superfluid helium (^{3}He), it was long believed that such topological states are rather exceptional in nature and exist only in quantum liquids under extreme conditions (under high magnetic fields or at very low temperatures). However, after the discovery of topological insulators (TIs), it has become evident that topological states of matter can actually be widespread. In this sense, TIs have established a new paradigm about topological materials. It is generally expected that studies of topological materials would deepen our understanding of quantum mechanics in solids in a fundamental way [6].

1.3 Field theoretical perspective

Two different approaches have been developed to provide unified characterization of gapped phases of free fermions. In the topological band theory approach, K-theory is applied to classify free fermion Hamiltonians in a given spatial dimension and symmetry class. The topological band theory provides a complete topological classification of free fermion gapped states in all dimensions and all the 10 Altland-Zirnbauer symmetry classes [7]. However, it does not directly describe physical properties

of the topological states. In comparison, the topological response theory approach describes topological phases by topological terms in their response to external gauge fields and gravitational fields. The advantage of this approach is that the topological phases are characterized by physically observable topological effects, so that the robustness of the topological phase is explicit and more general than in the topological band theory [8].

The key features regarding topological order may also be understood from a field theory perspective. Topological phases of matter are universally described by topological field theories, analogous to the way symmetry-breaking phases are described by field response theories [9]. Consider the quantum Hall effect. It turns out that a quantum Hall response results from coupling a $(2+1)$ dimensional massive Dirac equation to an external gauge field $\mathcal{A}$. Explicitly computing the linear part of the current-current correlation function shows that the Hall conductance equals $e^2/2\hbar\ \mathrm{sign}(m_t)$ in terms of the time-reversal breaking mass m_t. Hence, the system suffers an anomaly; even in the limit of vanishing mass, the resulting transverse conductance is non-zero. Further inspection shows that this essentially is the continuum version of the Haldane model, which also exhibits anomalous chiral movers as m_t changes sign. More importantly, after integrating out the massive fermions we indeed find a topological term governing the response

$$S_{cs} \sim \mathbb{C}_1 \int d\mathbf{r} \int dt\ \mathcal{A}_\mu \epsilon^{\mu\nu\rho} \partial_\nu \mathcal{A}_\rho \qquad\qquad \mu,\nu,\rho = \{0,1,2\}.$$

This effective action is known as the Chern-Simons term, and is manifestly topological due to the presence of the first Chern character $\mathbb{C}_1$ and the fact that it does not depend on the metric. The Chern-Simons term has been well studied in the 1980s in order to understand the details of axion electrodynamics. Essentially, it may endow particles with a flux,

allowing for excitations with fractional charge and statistics.

1.4 Topological band insulators

As the first class of materials identified to exhibit topological properties preserving time-reversal symmetry, TIs are characterized by the topological invariant called the $\mathbb{Z}_2$ index [10, 11]. In a topological insulator, spin-orbit coupling causes an insulating material to acquire protected edge or surface states that are similar in nature to edge states in the quantum Hall effect [12]. These edge states are protected by topology [13]. This can heuristically be related to the topology of knots. The non-trivial knotting of the energy bands of a topological insulator can then be represented by a non-trivial knot whereas a normal insulator is represented by a simple knot. In order to pass from a topological insulating phase to a trivial one the knot has to be cut open, straightened out and glued back together to obtain the trivial loop. The open ended string then represents the edge states providing for the unique signature of topology. This process is illustrated in Figure 1.2. The discovery of the topological insulator has led to the rise of the vast field of topological (semi-)metals.

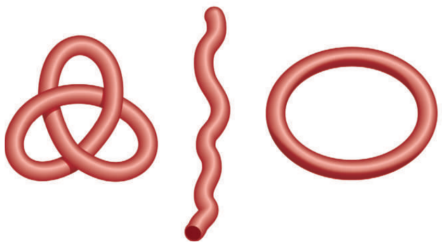

Figure 1.2: An illustration of topological change and the resultant surface state. The trefoil knot (left) and the simple loop (right) represent different insulating materials: the knot is a topological insulator, and the loop is an ordinary insulator. Because there is no continuous deformation by which one can be converted into the other, there must be a surface where the string is cut, shown as a string with open ends (centre), to pass between the two knots. Taken from [14].

1.5 Topological (semi)metals

Topological metals form the gapless cousins of topological insulators. Where the latter support a gapped spectrum, and gap closure means a topological phase transition, the former have a gapless spectrum, and gap opening requires a phase transition. The gaplessness of the topological metal is protected by topological charges in the Brillouin zone, i.e. points or more generally, submanifolds to which topological invariants may be assigned [15].

Semimetals such as Weyl semimetals represent such a topological phase, forming an intermediate state in the transition from metals to insulators, in which the conduction and valence band touch only at discrete points, leading to a zero band gap and singular points at the Fermi surface.

Although Weyl fermions were originally considered in massless quantum electrodynamics, and have not been observed as a fundamental particle

in nature, it has been theoretically understood that Weyl fermions can arise in similar semimetals exhibiting non-trivial topology [16, 17, 18], yielding the class of Weyl semimetals and thereby broadening the classification of topological phases of matter beyond that of insulators, as depicted in Figure 1.3.

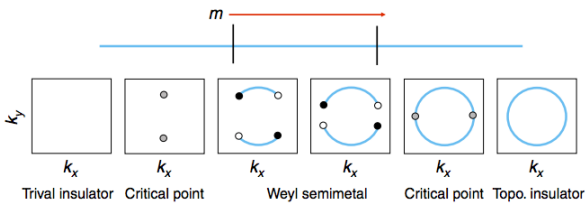

Figure 1.3: A Weyl semimetal can be understood as an intermediate phase between a normal insulator and a topological insulator as a function of a tuning parameter m. The grey circles represent the band touchings at the critical point, each of which is composed of two degenerate Weyl nodes. The black and white circles represent the Weyl nodes with positive and negative chiral charges. The blue lines represent the Fermi arcs.[19]

A Weyl semimetal exhibits an electronic band structure with singly degenerate bands that have bulk band crossings, called Weyl points. Around this Weyl points, it unveils a linear dispersion relation in all three momentum space directions when moving away from the Weyl point as shown in Figure 1.4. These materials can be viewed as an exotic spin-polarized, three-dimensional version of "graphene" that host topological Fermi arcs. The next chapter is dedicated to understanding the underlying mathematical structure of this topological phase of matter.

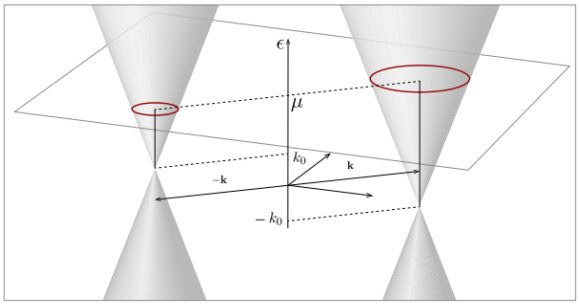

Figure 1.4: Two-dimensional schematic of the linearised dispersion relation characterizing a Weyl metal. Two (more generally, an even number of) Dirac cones, shifted relatively to each other both in momentum, $\pm\mathbf{k}$, and/or energy, k_0, are embedded into a 3D Brillouin zone. The ensuing topological Fermi surfaces defined by the chemical potential μ (shown as red circles) are Fermi spheres in 3D space. Adapted from [15].

1.6 Overview of thesis

A perturbation does not significantly change the properties of a fully gapped insulator, hence readily allowing us to define robust topological properties. Is it possible for a gapless system to have a defining topological feature? How can one distinguish phases of a system with gapless degrees of freedom that can be rearranged in many ways? In this work, we will consider a particular example of a gapless system that has drawn a lot of attention lately, Weyl semimetals.

There are three answers to the question of how such a gapless state can be topologically characterized despite the absence of a complete gap: in momentum space, the gapless points are 'topologically protected' by the behaviour of the band structure on a surface enclosing each point. There are topologically protected surface states, as in 3D topological insulators, which can never be realized in a purely two dimensional system. If a field is applied, there is a response whose value depends only on

the location of the gapless points, but on no other details of the band structure (and so is topological). Thus, characterising the topological behaviour of a Weyl semimetal and its response to a topological defect, in the form of a spatial dislocation, constitutes the main goal of this master research.

In order to achieve the latter, a detailed study of the theory of Weyl semimetals is required. Starting from the Dirac equation and Dirac semimetals, chapter 2 unveils the requirements for the transition to a Weyl semimetal, and its characteristic features such as the Weyl nodes and Fermi arc surface states and concludes by addressing the stability of the Weyl nodes to small perturbations.

Subsequently, the topological signature of Weyl nodes and their stability as monopoles of the Berry curvature is derived in chapter 3, accompanied by the relevant mathematical concepts covering the latter. Furthermore, the chiral anomaly, an anomaly known from particle physics, and recently revealed to be typical to Weyl semimetals, is studied.

As Weyl semimetals have attracted considerable attention in the physics world, due to their applications potential, chapter 4 is dedicated to giving a detailed overview of the experimental realisations of Weyl semimetals and the probing of their characteristics.

Having set the foundations of Weyl semimetals, the second half of this work is focused on the theory of lattice defects, in the form of dislocations, which is covered in chapter 5. This leads to the numerical part of this thesis in chapter 6, where the effect of a dislocation (or a π-flux) on the behaviour of different models of Weyl semimetals breaking either time-reversal symmetry or inversion symmetry, is studied.

Starting from tight-binding models that encode a topologically non-trivial phase, and analysing the corresponding continuum theory, de-

scribing the low energy excitations in the vicinity of the Weyl nodes in the Brillouin zone, we will answer the question whether the dislocation line (or vortex) and π-flux vortex, host a (or multiple) Kramers pair(s) of localized zero-energy dislocation modes. Based on the results found out of the computations, further dependences of the parameters of the models and their link to the response of the Weyl semimetals to dislocations is established. Finally, a possible interpretation of the results found is given and put in a broader context.

Chapter 2

Theory of Weyl semimetals

This chapter addresses the fundamental aspects of Weyl semimetals. Starting from the theory of Dirac semimetals, the transition to Weyl semimetals and its requirements is introduced. The typical features of Weyl semimetals are presented and the stability of the latter is discussed.

2.1 Dirac semimetals

Three-dimensional topological Dirac semimetals (DSMs) are a recently proposed state of quantum matter that have attracted increasing attention in physics and materials science. Understanding pseudo-Dirac-like fermions has become an imperative in modern condensed matter physics. All across its research frontier, from graphene to high T_c superconductors to topological insulators and beyond, various electronic systems exhibit properties which can be well-described by the pseudo-Dirac equation.

A 3D DSM is not only a bulk analogue of graphene; it also exhibits non-trivial topology in its electronic band structure that shares similarities with topological insulators. It represents an intermediate phase of matter between the latter and normal insulators, in which the conduction and valence band touch only at discrete points, leading to a zero band gap and singular points at the Fermi surface, called Dirac nodes. Moreover, a DSM can be driven into other exotic phases such as Weyl semimetals (WSM), which is the centre of interest of this research project, as well as axion insulators and topological superconductors, making it a unique parent compound for the study of these states and the phase transitions between them. The mathematical relation between a DSM and a WSM is explained in Appendix C. This relation raises the natural question: What are the criteria needed in order to physically go from a topological Dirac semimetal to a Weyl semimetal?

2.2 From a Dirac semimetal to a Weyl semimetal

Dirac nodes are described by four-component Dirac spinors satisfying the Dirac equation as shown in Appendix C, which can each be viewed as two two-component Weyl spinors with opposite chirality, as follows from the Nielsen-Ninomiya Theorem[1], satisfying the Weyl equation

$$i(\partial_0 - \boldsymbol{\sigma} \cdot \boldsymbol{\nabla})\psi_L = 0 \ , \ i(\partial_0 + \boldsymbol{\sigma} \cdot \boldsymbol{\nabla})\psi_R = 0.$$

The topological nature of Dirac semimetals lies in the fact that its nodes are protected locally by time-reversal symmetry, as well as inversion

[1] Nielsen-Ninomiya's theorem is treated in Subsection 3.5.

symmetry. Since, according to Kramer's theorem[2], all bands are doubly degenerate in case of the presence of time-reversal symmetry [20], Dirac nodes are thus themselves also degenerate. This results in a four-fold degeneracy of the Weyl fermions at each band crossing. The crystal symmetries of Dirac semimetals forbid the degenerate Weyl fermions to hybridise and open up a gap at each Dirac node [21].

In order to go from a Dirac semimetal to a Weyl semimetal, the breaking of time-reversal symmetry (TRS) and/or inversion symmetry (I) is required. The breaking of time-reversal symmetry causes each Dirac node to split into two separate Weyl nodes, of opposite chirality at opposite momenta $\pm\mathbf{k}_0$ since inversion symmetry requires that Weyl points at momentum $\mathbf{k}$ and -$\mathbf{k}$ have opposite topological charge. This can be done physically by doping a TI-NI multilayer[3] with magnetic impurities (This already has achieved in Bismuth-based TIs [22]). The breaking of inversion symmetry causes each Dirac node to split into two pairs of separate Weyl nodes of same chirality at opposite momenta $\pm\mathbf{k}_0$. This comes form the fact that if a Weyl node occurs at some momentum $\mathbf{k}$, time-reversal symmetry requires that another Weyl node occurs at -$\mathbf{k}$ with equal topological charge. It holds that the total topological charge associated with the entire Fermi surface must vanish. Hence, there must exist two more Weyl points of opposite topological at $\mathbf{k}'$ and -$\mathbf{k}'$ [64]. This can be realised within an asymmetric heterostructure or intrinsic inversion symmetry breaking. The implementation of these symmetry breakings in realistic materials is further elaborated in Chapter 4.

Breaking both symmetries leads to the creation of Weyl nodes at unspecified momenta (any $\mathbf{k}$) and having different energies, something that

[2] Kramer's theorem is stated and proven in Appendix B.1.

[3] A TI-NI multilayer is a multilayer system composed as a set of bilayers of a topological insulating system and a normal insulating system.

is experimentally hard to probe [23].

Table 2.1 resumes the different cases discussed above, for simplicity.

TRS present	I present	Implications	Min. number
×	×	Weyl nodes can be at any $\mathbf{k}$ and may have different energies.	2
✓	×	Weyl node at $\mathbf{k}_0 \iff$ Weyl node of same chirality at $-\mathbf{k}_0$.	4
×	✓	Weyl node at $\mathbf{k}_0 \iff$ Weyl node of opposite chirality at $-\mathbf{k}_0$	2
✓	✓	No stable, individually separated Weyl nodes possible.	none

Table 2.1: The implications of the presence or absence of time-reversal symmetry (TRS) and inversion symmetry (I) for Weyl nodes, along with the minimum number of Weyl nodes (if they are present at all). Adapted from [24].

2.3 Weyl nodes

Weyl fermions at zero energy correspond to points of bulk band degeneracy, Weyl nodes, which are associated with a chiral charge that protects gapless surface states on the boundary of a bulk sample. These surface states take the form of Fermi arcs connecting the projection of bulk Weyl nodes on the surface Brillouin zone [25].

Weyl semimetals were previously thought to have a point-like Fermi surface at the Weyl point. This type of Weyl semimetals has been classified as type-I, to distinguish them from the new type-II Weyl semimetals that exist at the boundaries between electron and hole pockets, as illustrated in Figure 2.1.

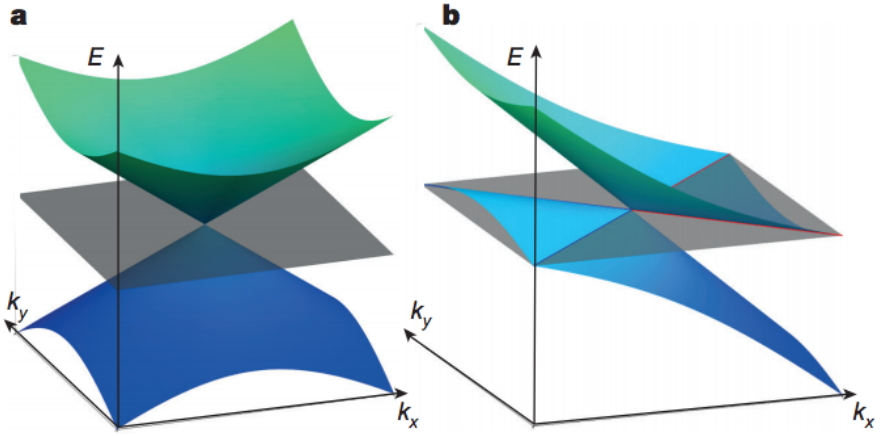

Figure 2.1: **Possible types of Weyl semimetals.** In plot a, a type-I Weyl point with a point-like Fermi surface. In plot b, a type-II Weyl point appears as the contact point between electron and hole pockets. The grey plane corresponds to the position of the Fermi level, and the blue (red) lines mark the boundaries of the hole(electron) pockets [26].

A general band theory can be written in terms of a quadratic Hamiltonian given by $H = \sum_{\alpha,k} \epsilon_\alpha(k) c_k^\dagger c_k$, where α indexes the bands. As a consequence of being Gaussian, the path-integral formalism can be used to show that high-energy modes can be integrated out and we are left with the modes of interest. The effective theory then is given by the low-energy limit of the Hamiltonian [27].

The $\mathbf{k} \cdot \mathbf{p}$ Hamiltonian describing the linear behaviour of such band-touching points takes the form of a (2×2)-Hamiltonian of a chiral Weyl fermion, hence the name Weyl semimetal. Each Weyl point can be identified with a hedgehog singularity of the Berry curvature, i.e. as a monopole of this k-space magnetic field. Weyl nodes of opposite chirality are connected by open Fermi arc surface states. The shape of these arcs depends on the boundary conditions of the semimetal and can be engineered. Together with the Fermi surface of bulk states, the Fermi

arcs on opposite surfaces form a closed Fermi surface. A schematic representation of the Weyl nodes and Fermi arcs in momentum space is given in Figure 2.2. The stability of the former is discussed in the next section.

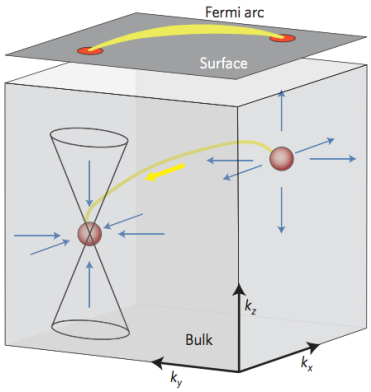

Figure 2.2: Schematic of the structure of the Weyl semimetal in momentum space. Two diabolical points are shown in red, within the bulk 3D Brillouin zone. Each Weyl node is a source or sink of the flux of the Berry connexion, as indicated by the blue arrows. The dark grey plane indicates the surface Brillouin zone, which is a projection of the bulk one. The Weyl nodes are connected by a Fermi arc, as shown by the yellow line. [18, 28]

2.4 Stability of Weyl nodes

To argue that a single Weyl node is stable to small perturbations regardless of symmetry, a well-known argument about level crossing in quantum mechanics can be applied [29]. Consider a pair of energy levels that approach each other. Of interest is studying when the crossing of these energy levels is allowed. Writing a general Hamiltonian for these two levels yields:

$$H = \begin{pmatrix} \delta E & \psi_1 + i\psi_2 \\ \psi_1 - i\psi_2 & -\delta E \end{pmatrix}.$$

The energy splitting is given by $\Delta E = \pm\sqrt{\delta E^2 + |\psi_1|^2 + |\psi_2|^2}$. In order to get $\Delta E = 0$, we need to individually tune each of the three real numbers to zero. This gives a set of three equations, which in general needs three variables for a solution. The 3D Brillouin zone provides three parameters which in principle can be tuned to find a node, using the Pauli matrices. While this does not guarantee a node, once such a solution is found, a perturbation which changes the Hamiltonian slightly only shifts the position of the solution in momentum space. Note that this does not yield the energy of the Weyl node, in some cases it is fixed a the chemical potential coming from other considerations.

Chapter 3

Topological signature of Weyl points

In this chapter, the mathematical signature of Weyl semimetals is studied and its relation to mathematical concepts such as the Berry curvature. We introduce concepts such as the Chern number and the Berry phase, Berry connexion and Berry curvature and show that Weyl semimetals can be thought of as monopoles of the latter. Subsequently, the chiral anomaly of particle physics is discussed in the context of Weyl semimetals as well as their topological stability.

3.1 Gauss-Bonnet and Chern numbers.

Geometry and topology were famously connected back in the middle of the 19^{th} century by the Gauss-Bonnet theorem:

$$\int_{\mathcal{M}} d^2\mathbf{x}\, K(\mathbf{x}) = 2\pi\chi_{\mathcal{M}}$$

where K is the Gaussian curvature of a 2-dimensional surface on a compact orientable 2-manifold $\mathcal{M}$ and $\chi_{\mathcal{M}}$ is the Euler characteristic, which is related to the genus[1] of the surface.

This remarkable relation evolved through mathematical abstraction to the one of Chern classes, where the first Chern class is given by

$$\int_{\mathcal{M}} dx^{\mu} dx^{\nu} \, \mathcal{F}_{\mu\nu}(\mathbf{x}) = 2\pi \mathbb{C}_1$$

where $\mathcal{F}_{\mu\nu}$ represents the Berry curvature, discussed in the next section, and $\mathbb{C}_1$ the first Chern class topological invariant. This topological invariant is central to systems with broken time-reversal symmetry, such as topological insulators and Weyl semimetals. The Berry curvature presented in the equation above and related concepts are derived in the next section.

3.2 Berry phase, Berry curvature and Berry connexion

In 1982, Berry's "geometric phase" exposed issues in "adiabatic quantum mechanics" that had previously been hidden due to implicit gauge fixing. Berry's phase is an example of holonomy, the extent to which some variables change when other variables or parameters characterising a system return to their initial values [30].

A quantum system being in a stationary state is described by a Hamiltonian $H(\mathbf{k})$. If the system is altered adiabatically, then according to

[1] Every connected, closed oriented surface is obtained from the 2-sphere S^2 by taking repeated connected sums with the torus, $T = S^1 \times S^1$. The number of tori added is a topological invariant called the genus.

the Adiabatic Theorem (Messiah [31]), the system will always be in an eigenstate of $H(\mathbf{k})$. If the Hamiltonian is returned to its original form, the system will return to its original state, apart from acquiring a phase factor known as the Berry phase [32]. Consider a state $|\psi(t)\rangle$ prepared in an initial eigenstate $|\psi(t_0)\rangle = |n(\mathbf{k}(t_0))\rangle$, evolving according to the parameter-dependent eigenstate $|n(\mathbf{k}(t))\rangle$, up to a phase. Then at a time t it holds that

$$|\psi(t)\rangle = e^{i\gamma_n(\mathbf{k}(t))} e^{-i\int_{t_0}^{t} dt' E_n(\mathbf{k}(t'))} |n(\mathbf{k}(t'))\rangle,$$

where the second exponential describes the time evolution of the state $|n(\mathbf{k}(t))\rangle$. The first phase represents an extra phase that accommodates for all effects beyond dynamical phases. Making use of the Schrödinger equation for the state $|\psi(t)\rangle$ we get

$$\gamma_n(\mathbf{k}(t)) = i\int_{t_0}^{t} dt' \ \langle n(\mathbf{k}(t'))|\frac{d}{dt'}|n(\mathbf{k}(t'))\rangle = i\int_{k(t_0)}^{k(t)} d\mathbf{k}' \ \langle n(\mathbf{k}')|\nabla_{\mathbf{k}'}|n(\mathbf{k}')\rangle.$$

In the Brillouin zone, for $\mathbf{k}(t_0) = \mathbf{k}(t)$, this results in a closed path in parameter space,

$$\gamma_n = i\oint_{\mathcal{C}} d\mathbf{k} \ \ \langle n(\mathbf{k})|\nabla_{\mathbf{k}}|n(\mathbf{k})\rangle$$

which represents the Berry phase. Using the Kelvin-Stokes theorem, it can be written as

$$\gamma_n = i\oint_{\mathcal{C}} d\mathbf{k}\cdot\langle n(\mathbf{k})|\nabla_{\mathbf{k}}|n(\mathbf{k})\rangle = i\oint_{\mathcal{C}} d\mathbf{k}\cdot\mathcal{A}_n(\mathbf{k})$$

where we introduced the Berry connexion $\mathcal{A}_n(\mathbf{k})$, representing a vector potential. This quantity is not invariant under the gauge transformation $|n(\mathbf{k})\rangle \to e^{i\phi_n(\mathbf{k})}|n(\mathbf{k})\rangle$ since we get: $\mathcal{A}_n(\mathbf{k}) \to \mathcal{A}_n(\mathbf{k}) - \nabla_{\mathbf{k}}\phi_n(\mathbf{k})$. Taking the curl of this quantity yields the well-known Berry curvature

$$\mathcal{F}_n(\mathbf{k}) = \nabla_{\mathbf{k}} \times \mathcal{A}_n(\mathbf{k})$$

and thus

$$\mathcal{F}_{n,\mu\nu}(\mathbf{k}) = \partial_\mu \mathcal{A}_{n,\nu}(\mathbf{k}) - \partial_\nu \mathcal{A}_{n,\mu}(\mathbf{k})$$

which represents a gauge invariant quantity. The Berry curvature can also be written, using linear response theory, as a sum over all other eigenstates in the form [30]

$$\mathcal{F}_{n,\mu\nu}(\mathbf{k}) = i \sum_{n' \neq n} \frac{\langle n|(\partial H/\partial k^\mu)|n'\rangle\langle n'|(\partial H/\partial k^\nu)|n\rangle - (\nu \leftrightarrow \mu)}{(\varepsilon_n - \varepsilon_{n'})^2}.$$

In order to conceive this graphically, a plot of the Berry curvature in momentum space is given in Figure 3.1.

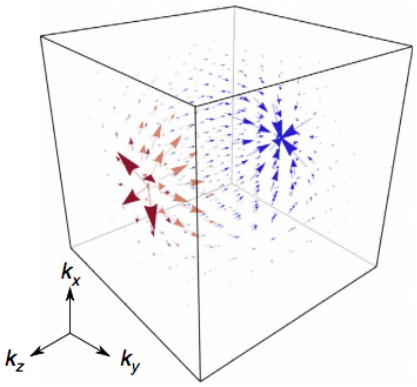

Figure 3.1: The vector plot of the Berry curvature in momentum space. The arrows show that the flux of the Berry curvature flows from one monopole (red) to the other (blue), defining the non-trivial topological properties of a topological semimetal. From [33].

Furthermore, the Berry Curvature and the quantum metric[2] are related by the inequality

$$\mathcal{G}_{\mu\mu}\mathcal{G}_{\nu\nu} - (\mathcal{G}_{\mu\nu})^2 \geq (\mathcal{F}_{\mu\nu})^2$$

[2]The quantum metric $\mathcal{G}_{\mu\nu}(\mathbf{x})$ on the manifold is the metric induced by the quantum metric in the full Hilbert space.

Now that the topological nature of the Berry curvature is elucidated, its relation to Weyl nodes, being the signature of topological Weyl semimetals, is derived in the next section.

3.3 Weyl points as monopoles of the Berry curvature

The topological signature of a Weyl node is mathematically proven by showing that it is a quantized source of the Berry flux.
In a Weyl semimetal, being a multi-band system, the electrons of the n^{th}-band are described by

$$\psi_n(\mathbf{k}) = \langle \mathbf{k} | n(\mathbf{k}') \rangle.$$

The Berry connexion and curvature of the n^{th}-band are given by:

$$\mathcal{A}_n(\mathbf{k}) = i\langle n(\mathbf{k}) | \nabla_{\mathbf{k}} | n(\mathbf{k}) \rangle \quad \text{and} \quad \mathcal{F}_n(\mathbf{k}) = \nabla_{\mathbf{k}} \times \mathcal{A}_n(\mathbf{k}).$$

Since the Berry curvature $\mathcal{F}_n$ is the curl of the vector field $\mathcal{A}_n$ it holds that

$$\nabla_{\mathbf{k}} \cdot \mathcal{F}_n(\mathbf{k}) = 0.$$

This however only holds as long as the steps above are well defined, the latter in particular as long as the n bands are non-degenerate. This does not hold in a Weyl semimetal since at the Weyl node at least two degenerate bands meet. Therefore, the Berry connexion and the Berry curvature are ill-defined at a Weyl node. For a Hamiltonian, describing a Weyl semimetal, of the form

$$H = a(\mathbf{k}) \mathbb{1}_{2\times 2} + b(\mathbf{k}) \cdot \sigma,$$

which is topologically equivalent to a spin in a magnetic field [24], it can be shown that the i^{th} component of the Berry curvature is given by

$$\mathcal{F}_i(\mathbf{k}) = -\frac{1}{8\pi}\frac{1}{|\mathbf{b}(\mathbf{k})|^3}\epsilon_{ijm}\ \mathbf{b}(\mathbf{k}) \cdot \frac{\partial \mathbf{b}}{\partial k_j} \times \frac{\partial \mathbf{b}}{\partial k_m}.$$

For right and left-handed Weyl Hamiltonians, where $\mathbf{b}(\mathbf{k}) = \pm v_F \mathbf{k}$, the Berry curvature thus reads

$$\mathcal{F}_{\text{RH}}(\mathbf{k}) = \frac{1}{4\pi}\frac{\mathbf{k}}{|\mathbf{k}|^3} \quad \text{and} \quad \mathcal{F}_{\text{LH}}(\mathbf{k}) = -\frac{1}{4\pi}\frac{\mathbf{k}}{|\mathbf{k}|^3}.$$

This leads to

$$\nabla_{\mathbf{k}} \cdot \mathcal{F}_{\text{RH}}(\mathbf{k}) = \delta(\mathbf{k}) \quad \text{and} \quad \nabla_{\mathbf{k}} \cdot \mathcal{F}_{\text{LH}}(\mathbf{k}) = -\delta(\mathbf{k}).$$

This shows that Weyl nodes are indeed monopoles of the Berry curvature. They thus are sources of quantized Berry flux in the momentum space. Their charges can be defined by the corresponding Chern numbers of ± 1 [34]. It is then natural to question the stability of the latter, a matter where topology comes into play, again.

3.4 Stability of Weyl nodes: topological perspective

The stability of Weyl nodes can also be viewed from a topological perspective: a characteristic feature of a 3D topological metal, which Weyl semimetals are part of, is the presence of two or more disconnected sheets of the Fermi surface. The Fermi sheet S_{na} of the Fermi surface S_n of band n is defined as the a^{th} connected isolated set of points $E_n(k) = E_F$. To each Fermi sheet corresponds a non-zero Chern number,

$$\mathbb{C}_{na} = \frac{1}{2\pi}\oint_{s_{na}} dS \mathbf{v}_F \cdot \mathcal{F}_{\mathbf{n}}(k)$$

where $\mathbf{v}_F$ is the unit normal to S_{na}. It holds, as Haldane pointed out [35, 17], that the sum of these Fermi surface Chern numbers is always zero to satisfy gauge invariance, due to the Nielsen-Ninomiya theorem (treated in Section 3.5) [36, 37, 38, 39]. More technically, this Chern number represents the first Chern class of the mapping between a 2-manifold S_i and the "U(1) principal bundle" (see Appendix A) defined by the k_F-dependent quasiparticle wavefunctions inside the unit cell [17]. The stability of Weyl nodes relates to the Chern number as follows: for any fixed non-zero value of k_z at which the energy band structure is gapped, a Chern number $\mathbb{C}_{k_z}$ can be defined on the 2D (k_x-k_y)-plane, as it is gapped. As k_z is varied, $\mathbb{C}_{k_z}$ can only change when the 2D (k_x-k_y)-plane crosses a Weyl point. We can thus assign to each Weyl point an integer ($\mathbb{Z}$) topological charge which is the change in $\mathbb{C}_{k_z}$ at the topological phase transition. The well-defined topological charge makes Weyl points stable. A non-trivial value of the Chern number also guarantees that there exist chiral surface states which form the Fermi arcs connecting projections of two Weyl points with opposite charges onto the surface Brillouin zone.

However, the topological stability of Weyl points is lost when both time-reversal and inversion symmetries are retrieved in the material, since the combination of the two symmetries constrains two Weyl points with opposite Chern numbers to merge, thereby making the total topological charge vanish and thus retrieving a Dirac semimetal [40].

Another feature of a Weyl fermion, since it obeys the Weyl equation, is that this Chern number is related to its chirality. The latter plays an important role, since in parallel electric and magnetic fields, charge is predicted to flow between the Weyl nodes of opposite chirality, lead-

ing to negative magnetoresistance. This "axial" current is the chiral (Adler-Bell-Jackiw) anomaly investigated in quantum field theory and is presented in the next section.

3.5 A quantum anomaly: the chiral anomaly

Quantum anomalies are the breaking of a classical symmetry by quantum fluctuations. They dictate how physical systems of diverse nature, ranging from fundamental particles to crystalline materials, respond topologically to external perturbations, insensitive to local details [41].

In 1983, Nielsen and Ninomiya proposed that the chiral anomaly descending from particle physics might be observable in a crystal with massless Weyl fermions in even space-time dimension (1+1 or 3+1). From there they formulated the no-go theorem(also known as the fermion doubling theorem) to relate this anomaly to condensed matter systems and particularly to describe the behaviour of Weyl fermions in crystals [36, 37, 38, 39].

3.5.1 Chiral anomaly as a result of QFT

The chiral anomaly is an unexpected feature of relativistic quantum field theories. A derivation of this anomaly for the case of Weyl semimetals is given in Appendix F.

If a massless fermion obeys the Dirac equation, the quasiparticle is expected to possess a definite physical quantity χ, its chirality, defined

as

$$\chi = h = \frac{\mathbf{s} \cdot \mathbf{p}}{|\mathbf{s}||\mathbf{p}|}$$

where h represents the helicity[3]. As established in Appendix C, the Dirac equation for massless particles possesses a chiral symmetry, no chirality is preferred and the two chiralities are not mixed.

This fails to hold when gauge invariance is taken into account. Chirality is no longer conserved when the fermions are placed into an electromagnetic field with co-linear magnetic and electric field components as pictured in Figure 3.4. This anomaly is known as the Adler-Bell-Jackiw anomaly, who observed it while trying to explain the decay of a neutral pion into two photons [42, 43], which had been the centre-stage of particle physics research. Although the decay rate was explained satisfactorily by Steinberger in 1949 in terms of triangle diagrams as in Figure 3.2, with a proton circulating in the fermion loop, problems arose

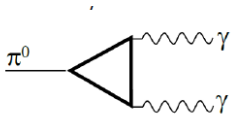

Figure 3.2: Scheme of the decay of a neutral pion π^0 into two photons γ. [42, 43]

sixteen years later, when decay rates obtained within the framework of current algebra and partial conservation of axial vector current were invariably smaller than the data obtainedby three orders of magnitude. Adler, Bell and Jackiw then independently established that the presence of the electromagnetic field engenders the coupling of the particles to the electromagnetic field $F_{\mu\nu}$ and the simultaneous creation of particles of definite chirality and antiparticles of the opposite one. This leads to

[3]Note that these two quantities are not equal in the case of a massive particle.

the the total charge being conserved but not the chirality. This means intuitively that a chiral charge is pumped from one branch to the other at a rate given by [44]:

$$W = \chi \frac{e^3}{4\pi^2\hbar^2} \, \mathbf{E} \cdot \mathbf{B}.$$

Recently, this chiral anomaly has been found to exist in condensed matter systems, a matter discussed in the next section.

3.5.2 Chiral anomaly in a condensed matter system

For any realistic lattice systems, the chiral anomaly manifests itself in the intervalley pumping of the electrons between Weyl points with opposite chirality. In the non-interacting case, the chiral anomaly can be simply ascribed to the zeroth Landau levels, which are chiral and have opposite signs of the velocity for states around Weyl points with opposite chirality, as can be seen in Figure 3.3. The zeroth Landau levels relate to the Weyl equation, discussed in Appendix C:

$$i(\partial_0 - \boldsymbol{\sigma} \cdot \boldsymbol{\nabla})\psi_L = 0 \ , \ i(\partial_0 + \boldsymbol{\sigma} \cdot \boldsymbol{\nabla})\psi_R = 0.$$

Here $\psi_{R,L}$ represent two 2-spinors with definite opposite chirality as shown in figure 3.3.

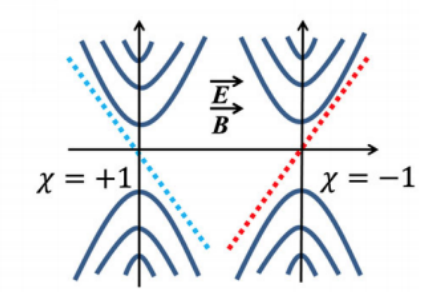

Figure 3.3: **Schematic diagram of bulk Landau levels of a pair of Weyl nodes.** The dotted lines represent the zeroth quantum Landau level with positive (blue) and negative (red) chiralities in a magnetic field parallel to the electric current. Taken from [19].

The additional presence of an electric field parallel to the magnetic field will generate charge imbalance between two chiral nodes, leading to an electric current that can only be balanced by intervalley scattering as can be seen in Figure 3.4.

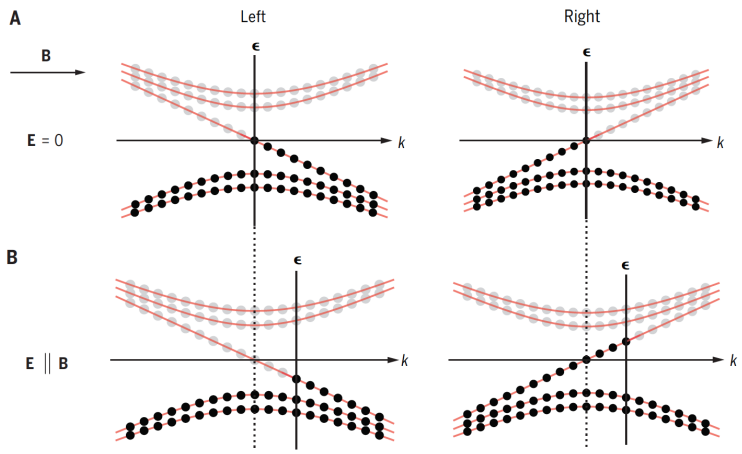

Figure 3.4: **Illustration of the chiral anomaly.** Plot (A) represents the energy spectrum of the left- and right-handed fermions in the presence of a magnetic field **B**. The quantization of the field yields a zeroth Landau level. The filled states with negative energy (the Dirac sea) are represented by black dots and empty states with positive energy are represented by grey dots. Plot (B) represents the additional presence of an electric field **E** || **B** resulting in the production of right-handed particles and left-handed antiparticles and a shift in the filling. For all plots, ϵ represents the energy and k the wave-vector. Taken [45].

Chapter 4

Realisations in materials

In this chapter, the experimental realisations of Weyl semimetals are presented. The potential materials are discussed and the different techniques to break the relevant symmetries are studied. The topological properties of Weyl semimetals are probed by observing the Weyl nodes and surface states as well as the chiral anomaly through negative magnetoresistance.

As previously mentioned, in order to experimentally obtain a Weyl semimetal state of matter, and to be able to probe this accordingly, either time-reversal symmetry or inversion symmetry have to be broken. Time-reversal symmetry breaking can be achieved by magnetic doping. Therefore, the early predictions of Weyl semimetals did focus on magnetic materials, like $R_2Ir_2O_7$ and $HgCr_2Se_4$, which naturally break this symmetry. However, due to the intricate magnetic domain structure of the samples, the experimental verification of these compounds still remains a challenge.

On the other hand, inversion symmetry breaking has attracted a lot of attention recently through non-centrosymmetric transition metal monoarsenides and phorsphides such as TaAs, NbAs, TaP and NbP, which have been proposed as potential Weyl semimetal candidates [46]. These compounds spontaneously break the inversion symmetry due to their geometrical structure [47], while avoiding the complication of working with correlated materials with magnetic ground states, which is ideal for angle-resolved photo-emission spectroscopy (ARPES) measurements.
This chapter presents a couple of Weyl semimetal (potential) materials and the methods used to probe them. Characterising the topology of the Weyl semimetals by experimentally verifying and detecting the Weyl nodes, the cones and the corresponding Fermi arcs surface states represents the main focus of these experiments as well as measuring the chiral anomaly predicted by Nielsen-Ninomiya.

4.1 Experimental predictions and observations of the topology of Weyl semimetals: Cones, points and Fermi arcs

Several groups have reported the direct observation of the bulk Weyl points and the surface Fermi arcs by ARPES, confirming these compounds as topological Weyl semimetals.

4.1.1 Pyrochlore iridates

Some of the most striking condensed matter phenomena, such as high-temperature superconductivity and colossal magnetoresistance, were found in transition metal systems involving $3d$ orbitals with strong electron correlations. Now it has been realized that in $4d$ and $5d$ systems, such as pyrochlore iridates (PIs), where orbitals are spatially more extended, a regime of intermediate correlation appears. These materials display significant spin-orbit coupling, which modifies their electronic structure. Furthermore, PIs have recently been attracting considerable attention because of their novel transport properties such as the anomalous Hall effect in $Nd_2Mo_2O_7$, superconductivity in $Cd_2Re_2O_7$ and AOs_2O_6. (A = K, Rb, and Cs), and the under-screened Kondo effect in $Pr_2Ir_2O_7$. They represent one of the first candidates for the experimental realisation of a Weyl semimetal as Wan *et al.*[16] have found for the compound $Y_2Ir_2O_7$ using LSDA+U +SO[1] calculations in a range of parameters appropriate to the iridates, where all energy scales are comparable. The calculated Weyl nodes are shown in figure 4.1.

[1] LSDA stands for local-spin-density approximation, U represents chemical potential and SO stands for spin orbit

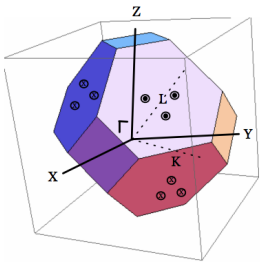

Figure 4.1: The low energy physics of pyrochlore iridates is described by linearly dispersing fermionic modes near nodes in the band structure. The position of Weyl nodes in the Brillouin zone is shown in the figure. There are three nodes, with the same chirality, located in the vicinity of the L points, and nodes related by inversion have opposite chirality. From [48].

4.1.2 Tantalum Arsenide (TaAs)

Tantalum arsenide is a semi-metallic material that crystallizes in a body-centred tetragonal lattice system. It is constructed by inter-penetrating Ta and As sublattices, such that they are shifted with respect to each other.

Using soft x-ray (SX) and ultraviolet (UV) angle-resolved photo-emission spectroscopy (ARPES) techniques, both the surface and bulk electronic structure of TaAs have been studied and the 3D Weyl nodes, Weyl cones and Fermi arc surface states have been identified.

Superimposing the data obtained using both independent methods demonstrated that terminations of the Fermi arcs correspond to the projected Weyl nodes which proves the topological nature of the Weyl semimetal (the surface-bulk correspondence)[25].

4.1.3 Gyroid photonic crystals

In the context of gyroid photonic crystals, another approach was chosen, namely to break inversion symmetry instead of time-reversal symmetry to avoid using lossy magnetic materials and external magnetic fields [34]. Through this method, the experimental probing of Weyl nodes can be extended to photonic crystals at optical wavelengths. The materials of choice were slabs of ceramic-filled plastics. A single gyroid structure can be approximated by drilling periodic air holes along the x, y, and z directions. The 3D double gyroid structure can be made by stacking layers of two gyroid inversion counterparts that interpenetrate each other as can be seen in Figure 4.2. Modifying the vertical connexions of one of the gyroid layers results in the breaking of inversion symmetry. In order to probe the dispersion of the 3D bulk states and the Weyl nodes, angle-resolved transmission measurements were performed on the photonic crystal sample [34].

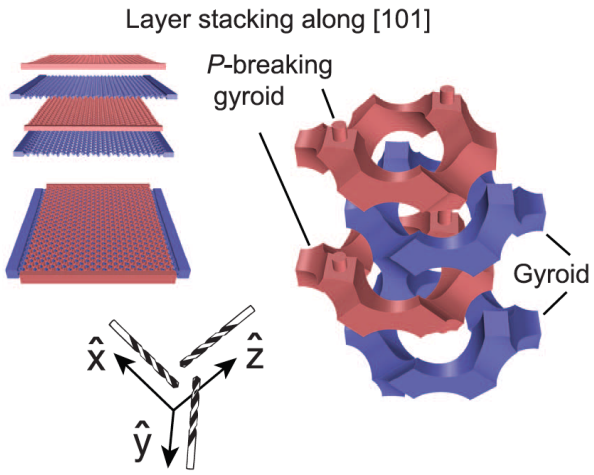

Figure 4.2: The 3D double gyroid structure can be made by stacking layers along the [101] direction. The red and blue gyroids, being inversion counterparts, interpenetrate each other. The vertical connexions of the red gyroid are shrank to thin cylinders in order to break inversion symmetry. Taken from [34].

Once the topological signature had been characterised and Weyl semimetals discovered, the interest for the chiral anomaly and its experimental observation considerably grew.

4.2 Experimental observation of the chiral anomaly in Weyl semimetals

4.2.1 Negative magnetoresistance

Negative magnetoresistance is the term given to the large decrease in the electrical resistance when a system is exposed to a magnetic field. The (negative) magnetoresistance (MR) is usually defined as a percentage

ratio [49]:

$$MR = \frac{\rho(H) - \rho(0)}{\rho(0)} \times 100\%$$

where ρ represents the resistivity.

Considering the fact that for clean samples the intervalley scattering time is extremely long and the degeneracy of the Landau level is proportional to the magnetic field strength, the chiral anomaly in a Weyl semimetal will in general lead to a negative magnetoresistance when the magnetic field is parallel to the current [33]. There even exists a critical value of the magnetic **B**-field for each temperature, below which a pronounced negative magnetoresistance is observed even with temperature up to $300K$ as we can see in figure 4.3 [33]. In this experiment, the response of the semimetal to different fields **E** and **B** has been checked.

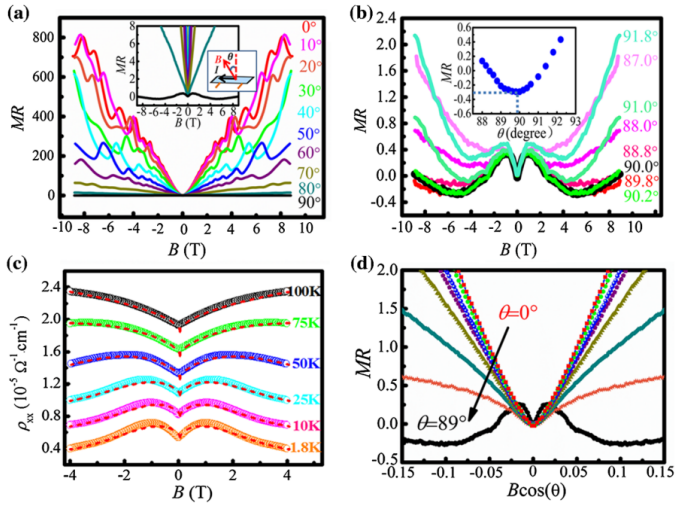

Figure 4.3: Angular and field dependence of MR in a TaAs single crystal at 1.8 K. (a) Magnetoresistance with respect to the magnetic field (**B**) at different angles between **B** and the electric current (**I**) ($\theta = 0° - 90°$). The inset zooms in on the lower MR part, showing negative MR at $\theta = 90°$ (longitudinal negative MR), and it depicts the corresponding measurement configurations. (b) Magnetoresistance measured in different rotating angles around $\theta = 90°$ with the interval of every 0.2°. The negative MR appeared at a narrow region around $\theta = 90°$, and most obviously when $\mathbf{B} \parallel \mathbf{I}$. Either positive or negative deviations from 90° would degenerate and ultimately kill the negative MR in the whole range of the magnetic field. Inset: The minima of MR curves at different angles ($88° - 92.2°$) in a magnetic field from 1 to 6 T. (c) The negative MR at $\theta = 90°$ (open circles) and fitting curves (red dashed lines) at various temperatures. $T = 1.8, 10, 25, 50, 75$ and $100K$. (d) Magnetoresistance in the perpendicular magnetic field component, $\mathbf{B} \times \cos(\theta)$. The misalignment indicates the 3D nature of the electronic states. From [19].

Chapter 5

Topology of lattice defects

This chapter covers the topology of lattice defects in the context of dislocations. At first, dislocations and related concepts such as the Burgers vector are introduced. Subsequently, the effect of the former on the lattice band structure is studied according to the **K-b-t***-rule and related to the case of Weyl semimetals. At last, concepts such as edge states and effective flux are introduced.*

Topological defects, such as domain walls and vortices, have long fascinated physicists and are . A novel twist is added in quantum systems such as the B-phase of superfluid helium ^{3}He and ^{4}He [50], where vortices are associated with low-energy excitations in the core. In this case, the order-parameter fields of the superfluid phases of ^{3}He and ^{4}He not only allow for planar defects but also for point and line-like defects, (called "monopoles" and "vortices", respectively). Defects can be "non-singular" or "singular", depending on whether the core of the defect remains superfluid or whether it is forced to become normal liquid [51].

Similarly, topological defects in the field of cosmic strings may be tied to propagating fermion modes as in the case of a single soliton [50, 52]. The natural question arises whether analogous phenomena can occur in crystalline solids hosting a plethora of topological defects. As dislocations are ubiquitous in real materials, these excitations could influence spin and charge transport in Weyl semimetals. In contrast to fermionic excitations in a regular quantum wire, these Weyl nodes are topologically protected and thus not scattered by disorder [50].
The notion of dislocations as a topological defect is presented in the next section.

5.1 Dislocations: a topological defect

A dislocation can be understood as a topological defect within the crystal structure, marking the boundary between a slipped and an unslipped region of a material, or, more intuitively, as a mismatch in the lattice structure. An illustration can be seen in figure 5.1. It can be obtained by virtually cutting into the crystal lattice along a plane and then gluing it back together with a translation or a twist in a way that away from the defect itself, the lattice parts are coordinated following the Volterra construction [53]. This results in a dislocation or a disclination (also called edge or screw dislocations, respectively) as can be seen in Figure 5.1 [54]. The concept of a dislocation in a solid was developed mathematically by Volterra in the early twentieth century [53], through his study of elastic deformations. It is based on the idea that internal stresses can arise from a relative misalignment in the crystal and may therefore be described accordingly.
For realistic materials we distinguish between (3+1)D and (2+1)D dis-

locations. To start with, consider a two dimensional lattice of a perfect crystal lattice. In order to create a dislocation, the lattice is endowed with a one dimensional line $\mathbf{v}$, ending at the point where the defect is to be created. This results in the displacement of the crystal at one side of the line $\mathbf{v}$, by a lattice vector called the Burgers vector $\mathbf{b}$, due to the addition (or removal) of atoms. The Volterra construction concludes by imposing the reconnection of the two parts of the crystal structure again. As a result, the crystal pieces get back along the whole "Volterra" cut except at the point defect $\mathbf{v}$, producing the desired point defect as can be seen in figure 5.2. Extrapolating this method to three dimensions, in order to create a dislocation, a perfect crystal lattice is enriched with a 2D plane $\mathbf{u}$ that ends at a curve $\mathbf{R}(\sigma)$, parametrising the line where the defect is to be produced as can be seen in the left panel figure 5.1. Reconnecting the two parts of the crystal structure results in the displacement of the crystal at one side of the plane $\mathbf{u}$ by the Burgers vector $\mathbf{b}$. This type of dislocation is called an edge dislocation. In this case, the Burgers vectors $\mathbf{b}$ is chosen parallel to the line defect $\mathbf{R}(\sigma)$. Choosing the Burgers vector perpendicular to the line defect $\mathbf{R}(\sigma)$ results in "cutting" the crystal structure along the plane $\mathbf{u}$ and "regluing" it together with a displacement equal to $\mathbf{b}$. This type of dislocation does not involve the removal or addition of atoms as can be been in the right panel of figure 5.1 and is referred to as a screw dislocation. These dislocations exhaust the possible topological defects that can be present in a crystal structure [54]. As mentioned before, they relate to the Burgers vector, which is introduced in the next section.

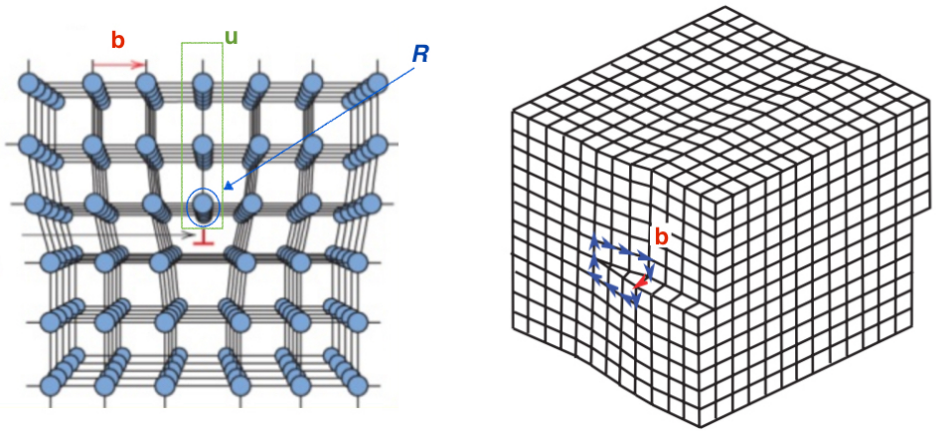

Figure 5.1: **Edge and screw dislocations in a cubic lattice.**
Right panel: Edge dislocation. The dislocation line $\mathbf{R}(\sigma)$ is situated in the middle of the front view. The Burgers vector **b** is indicated with an arrow. Starting with the perfect crystal, a plane**u** perpendicular to **b** beginning at the bottom plane and terminating at $\mathrm{R}(\sigma)$ is chosen. Removing one row of atoms at the lower side of the plane **u** and then 'gluing' the crystal back together results in the dislocation line $\mathbf{R}(\sigma)$.
Left panel: Screw dislocation. The Volterra construction is analogous to the edge dislocation case with the exception that in this case the Burgers vector **b** runs parallel to the plane **u**, which cuts the cubic crystal horizontally from the right side to the middle of the crystal. Translating the lower side of the crystal by one crystal unit in the **b** direction results in the screw dislocation.

5.2 Burgers vector

The Burgers vector associated with a dislocation is a measure of the lattice distortion caused by the presence of the line defect. Figure 5.2 shows the convention for measuring the Burgers vector. A loop is made around a dislocation line in a clockwise direction with each step of the loop connecting lattice sites that are fully coordinated. This loop is then transferred onto a perfect lattice of the same type. Because of the absence of a dislocation within this lattice, the transferred loop fails to close on itself, and the vector linking the end of the loop to the starting point is the Burgers vector, **b**. The Burgers vector defined in this way is a unit vector of the lattice if the dislocation is a unit dislocation, and a shorter stable translation vector of the lattice if the dislocation is a partial dislocation. Moreover, the Burgers vectors are additive, and in full generality we can thus consider only dislocations with the Burgers vectors equal to Bravais lattice vectors.

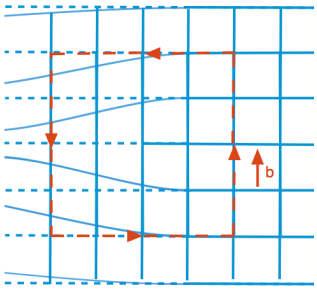

Figure 5.2: **A dislocation in a square lattice and its corresponding Burgers vector.** The original lattice is indicated with dashed lines. A closed loop (red) is made around the dislocation in a clockwise direction. The extra row of atoms results in a non-closure of the loop that, if transferred onto a perfect lattice, is exactly represented by the Burgers vector **b**.

The effect of the dislocation, being the translation by the Burgers vector $\mathbf{b}$, results in the multiplication of the wave-function $|\Psi_{\mathbf{k}}\rangle$ by a phase factor $e^{i\mathbf{k}\cdot\mathbf{b}}$. It is clear from this phase factor that $\mathbf{k}$ has to be finite in order for the dislocation to have an effect. This means that for the three dimensional case, for $\mathbf{k} = (k_x, k_y, k_z) = (k_x, 0, 0)$ where $k_x \neq 0$, a dislocation along the y-direction would result in an additional phase factor since the dislocation line runs parallel to the y-direction, yielding a Burgers vector $\mathbf{b} = be_{\mathbf{x}}$. On the other hand, a dislocation in the y- or z- direction would not affect the topology of the lattice structure.
Additionally, a dislocation is expected to disturb the crystalline order only microscopically close to its core. Therefore, expansion around the Weyl nodes should pertain to an effective elastic continuum theory.Furthermore, the orientation of the Burgers vector with respect to the dislocation line suggests a more profound relation between topology and geometry. These effects are captured within the **K-b-t** rule as presented in the next section.

5.3 The K-b-t rule

Dislocations represent a universal observable of translationally-active topological phases and the means of probing the interplay between topology and geometry. This section elucidates the general rule governing the response of dislocation lines in three-dimensional topological phases of matter following the work of Slager [54]. Although the latter is focused on the response of dislocation lines in topological band insulators, the **K-b-t** rule can be appropriately applied to the case of dislocation lines in Weyl semimetals.
According to this rule, the lattice topology, represented by dislocation

lines oriented in the direction $\mathbf{t}$ having Burgers vector $\mathbf{b}$, unites with the electronic band topology, characterized by the Weyl nodes' momentum $\mathbf{K}$, to produce an explicit criterium for the formation of gapless propagating modes along these line defects. Most interestingly, the general principles also identify that, for sufficiently symmetric crystals, this interplay leads to topologically-protected metallic states bound to freely deformable dislocation channels, that can be arbitrarily embedded in the parent system.

Dislocations in three dimensions represent defects with a far richer structure than their two-dimensional counterparts. They form lines $\mathbf{R}(\sigma)$ characterized by a tangent vector $\mathbf{t} \equiv d\mathbf{R}/d\sigma$, with the discontinuity introduced to the crystalline order described by the Burgers vector $\mathbf{b}$. Both vectors can only be oriented along the principal axes of the crystal, and edge (screw) dislocations are obtained when $\mathbf{b} \perp \mathbf{t}$ ($\mathbf{b}||\mathbf{t}$).

A crucial fact is the observation that translational lattice symmetry is preserved along the defect line for any proper dislocation probing the specific crystal geometry. Therefore, the full lattice Hamiltonian in the presence of a dislocation oriented along, for instance, the z-axis ($\mathbf{t} = \mathbf{e}_z$) can be written as

$$H_{3D}(x, y, z) = \sum_{k_z} e^{ik_z z} H^{2D}_{\text{eff}}(x, y, k_z).$$

Notice that the 2D lattice Hamiltonian H^{2D}_{eff} possesses the symmetry of the crystallographic plane orthogonal to the dislocation line, because the Burgers vector is a Bravais lattice vector. This directly confirms the universal status of the dislocation as the translational probe of the lattice topology.

As mentioned before, due to the locality of the effect of a dislocation on the lattice crystalline order, elastic continuum theory can be used

to describe its effect at low energies [55]. The elastic deformation of the continuous medium is encoded by a distortion field ϵ_i of the global Cartesian reference frame $\mathbf{e}_i$, $e_i^\alpha = \delta_i^\alpha$ with $i, \alpha = 1, 2, 3$ [55]. The momentum near the band gap closing at the momentum $\mathbf{K}$ is then $k_i = (\mathbf{e}_i + \boldsymbol{\varepsilon}_i) \cdot (\mathbf{K} - \mathbf{q})$ where $\mathbf{q} \ll \mathbf{K} \sim 1/a$, as the momentum of the low-energy electronic excitations $\varepsilon \sim a/r$ with a the lattice constant and r the distance from the defect core [55]. Therefore the dislocation gives rises to a $U(1)$ gauge fields $A_i = -\boldsymbol{\varepsilon}_i \cdot \mathbf{K}$ that minimally couples to the electronic excitations $\mathbf{q} \to \mathbf{q}+\mathbf{A}$. Due to the translational symmetry, the gauge field then has non-trivial components only in the plane orthogonal to the dislocation line, $\mathbf{A} \cdot \mathbf{t} = 0$ and

$$\mathbf{A} = \frac{-y\mathbf{e}_x + x\mathbf{e}_y}{2\pi r^2}(\mathbf{K}_{\text{inv}} \cdot \mathbf{b}) \equiv \frac{-y\mathbf{e}_x + x\mathbf{e}_y}{2\pi r^2}\boldsymbol{\Phi}$$

where $\boldsymbol{\Phi}$ represents an effective flux $\boldsymbol{\Phi} = \mathbf{K} \cdot \mathbf{b}$ as can be seen in Figure 5.3.

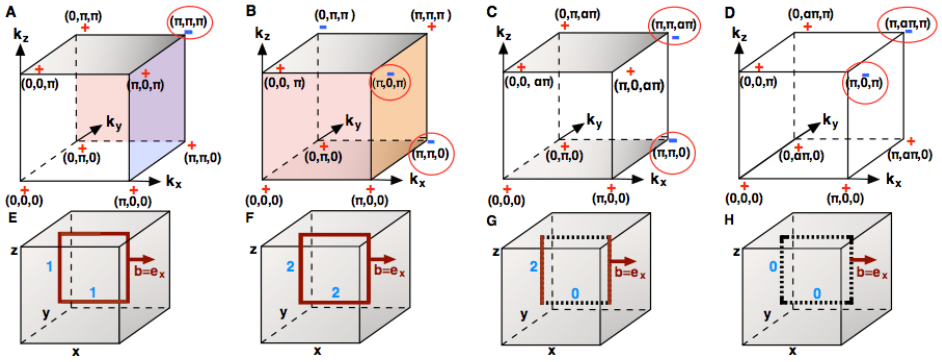

Figure 5.3: **Illustration of the K-b-t rule relating the electronic topology in the momentum space (top panels), and the effect of dislocations in real space (bottom panels).**

Panel A to D show the electronic band topology. A dislocation with Burgers vector $\mathbf{b} = e_{\mathbf{x}}$ acts on the encircled TRI momenta in the planes orthogonal to the dislocation line. As a result, the coloured planes host an (in this case) effective π-flux. As a result, the coloured planes host an effective π-flux. The resulting number of Kramers pairs of helical modes along the edge and screw parts of the loop is indicated with the blue number. (A) The symmetric phase has a topologically non-trivial plane hosting a π-flux orthogonal to any of the three crystallographic directions and hence any dislocation loop binds modes along the entire core, as shown for a loop in the x-z plane, panel E. (B) In this phase, translationally active phases in the TRI planes orthogonal to k_z and a valley phase in $k_x = \pi$ plane host π fluxes. Hence the dislocation loop binds two pairs of modes, as displayed in panel F. These modes are symmetry-protected against mixing. (C) In this phase, only the TRI planes normal to k_z host an effective π-flux and hence the same dislocation loop binds modes only to the edge-dislocation parts, as displayed in panel G. These modes are not protected against mixing. (D) In this phase, all TRI planes orthogonal to the dislocations lines have a trivial flux, and, according to the **K-b-t** rule, neither the edge nor the screw dislocation of the loop binds modes, as illustrated in panel H. Adapted from [54].

5.4 Effective flux and electromagnetic response

Weyl nodes represent monopole sources and sinks of the Berry curvature $\mathcal{F}_{\mu\nu}$ in k-space as shown in section 3.3. Therefore, the flux of $\mathcal{F}_{\mu\nu}$ through a surface enclosing such a node in k-space is quantized to the total topological charge enclosed. The Berry curvature can be regarded as an effective pseudo-magnetic field. This means that if we surround a Weyl node by a Gaussian surface S, the Chern flux captured defines the chirality

$$\chi = \frac{1}{2\pi} \oint_S \mathcal{F}(\mathbf{k}) \cdot d\mathbf{S}(\mathbf{k}).$$

The presence of this Berry curvature due to time-reversal symmetry breaking gives rise to a transverse "anomalous" velocity $v_A = \mathbf{F} \times e\mathbf{E}$ to a wave-packet, which might host novel transport features.

The electromagnetic response of Weyl semimetals to fields $\mathbf{E}$ and $\mathbf{B}$ has been studied thoroughly [56, 57, 58] and their universal topological response is given by the θ-term

$$S_\theta = \int dt d\mathbf{r}\, \theta(t, \mathbf{r})\, \mathbf{E} \cdot \mathbf{B}$$

where we used natural units. The axion-like field $\theta(t, \mathbf{r})$ is given by

$$\theta(t, \mathbf{r}) = 2(\mathbf{b} \cdot \mathbf{r} - b_0 t).$$

This unusual response is a consequence of the chiral anomaly [39, 59] and is derived in Appendix F. The physical manifestations of the θ-term can be best understood from the associated equations of motion, which

give rise to the following charge density and current response [60]

$$\begin{aligned} \rho &= \frac{e^2}{2\pi^2}\,\mathbf{b}\cdot\mathbf{B} \\ j &= \frac{e^2}{2\pi^2}\,(\mathbf{b}\cdot\mathbf{E} - b_0\mathbf{B}). \end{aligned}$$

5.5 Edge states

Topologically non-trivial bulk phases commonly have robust edge states on their boundaries with topologically-trivial regions such as the vacuum as can be seen in figure 5.4. The physical interpretation of this anomaly is more subtle for the Weyl semimetal than for the the topological band insulator. In the latter case, due to the bulk gap, the anomaly means that there is a helical zero mode on the dislocation. In the Weyl semimetal case, there is no bulk gap. Furthermore, if the region carrying a non-zero Chern number is near $k_z = 0$, then that region sees only small perturbations from the dislocation because the dislocation acts like a flux proportional to k_z. Hence we should not necessarily expect a zero mode as an effect of the dislocation. The existence of such a zero energy dislocation mode is studied in the next chapter.

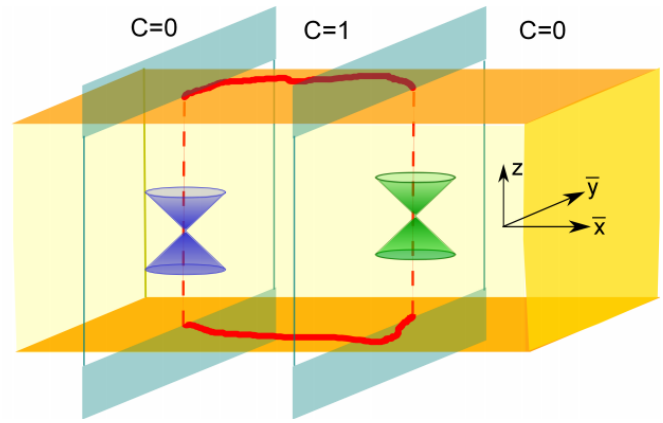

Figure 5.4: Weyl semimetal with a pair of Weyl nodes of opposite chirality (denoted by different colours green and blue) in a slab geometry. The surface has unusual Fermi arc states (shown by red curves) that connect the projections of the Weyl points on the surface. C is the Chern number of the 2D insulator at fixed momentum along the line joining the Weyl nodes. The Fermi arcs are nothing but the gapless edge states of the Chern insulators strung together. Form [61].

Chapter 6

Numerics

This chapter includes the main results of this project. Starting from two tight-binding models that respectively break time-reversal symmetry and inversion symmetry, the Weyl semimetal is encoded onto a lattice and studied. The effect of the presence of a π-flux and dislocations in the crystal lattice on the band structure is studied and the hypothesis based on the analysis of the results is presented.

Lattice dislocations can readily be included in numerical tight-binding calculations by adding extra atoms to the underlying lattice, as has been established in chapter 5. Starting from a tight-binding model that encodes a topologically non-trivial phase, the effect of a dislocation in the corresponding continuum theory, describing the low energy excitations in the vicinity of the Weyl nodes in the Brillouin zone, is studied. Additionally, the effect of the presence of a π-flux is elucidated.
For a spatial dislocation in the crystal lattice, consider a closed loop around the former. This loop translates into a non-closed loop onto

the original perfect lattice. This non-closure yields the Burgers vector $\mathbf{b}$ as established in 5.2. Note that this procedure pertains to loops of arbitrary size. Therefore, the effect on the wave-functions is global and long-ranged.

The effect of the dislocation, thus being this translation by the Burgers vector $\mathbf{b}$, results in the multiplication of the wave-function by a phase $\mathbf{\Phi} = \mathbf{k} \cdot \mathbf{b}$.

Keeping this in mind, in order to study the impact of dislocations in a Weyl semimetal, we proceeded to encode the relevant information into Mathematica by mapping different Hamiltonians describing Weyl semimetals onto a lattice.

Putting a Hamiltonian onto a lattice and being able to add lattice dislocations, requires us to work in $D \geq 1$ spacial dimensions, in order for the lattice coordinates to be well-defined in position space. For this, we construct a $2 \times (n_x \times n_y \times n_z)$-matrix where every entry in the matrix represents a specific coordinate (x_i, y_i, z_i) and where the two-fold degeneracy reflects what orbital is present at the coordinate (p or s-orbitals). We consider nearest-neighbour interactions only. The nearest neighbours are formed into pairs, from which one electron can hop from one site to the other, which would represent an entry in the matrix.

Starting from a tight-binding hopping Hamiltonian of spin-1/2 electrons, which are created at site r by $c^{\dagger}_{r,\sigma}$ number density per spin projection is $n_{r,\sigma} = c^{\dagger}_{r,\sigma} c_{r,\sigma}$. The models studied are defined on the cubic lattice, possess particle-hole symmetry and represent non-interacting Weyl semimetals. The computations are focused on two different models for Weyl semimetals, one breaking time-reversal symmetry and one breaking inversion symmetry.

6.1 Weyl semimetal models

Starting from the Hamiltonian for a Dirac semimetal:

$$H(\mathbf{k}) = \sum_{\mathbf{k}} \left[\epsilon_{\mathbf{k}} + 2t \sin(k_i)\sigma^i\right] c^\dagger_{\mathbf{k}} c_{\mathbf{k}}$$

where $c^\dagger_{\mathbf{k}}$, $c_{\mathbf{k}}$ and $\epsilon_{\mathbf{k}}$ represent the creation and annihilation operator and the on-site energy, respectively. The hopping term between sites is given by t and summation over $i = x, y, z$ is implied. Breaking the inversion symmetry of this model will give rise to a Weyl semimetal exhibiting a minimum of 4 Weyl nodes, as explained in chapter 2.

6.1.1 Model I: Breaking inversion symmetry

In order to go from the model for the Dirac semimetal to the one of a Weyl semimetal, we introduce a field that breaks inversion symmetry of the form $\mathbf{b} \cdot \boldsymbol{\sigma}$ with $\mathbf{b} = (-\sin k_{x_0}, 0, -\sin k_{z_0})$. This results in the following Hamiltonian for the Weyl semimetal

$$\begin{aligned} H(\mathbf{k}) = \sum_{\mathbf{k}} \big[\epsilon_{\mathbf{k}} &+ 2t(\sin(k_x) - \sin(k_{x_0}))\sigma_x + 2t\sin(k_y)\sigma_y \\ &+ 2t(\sin(k_z) - \sin(k_{z_0}))\sigma_z\big] c^\dagger_{\mathbf{k}} c_{\mathbf{k}} + h.c. \end{aligned} \tag{M1}$$

The on-site energy $\epsilon_{\mathbf{k}}$ is for simplicity set to 0 since a non-zero value would merely result in an energy shift of the bands and thus does not alter the physics of the system. The hopping term t is set to 1 for all three directions. Clearly, this Hamiltonian breaks inversion symmetry since $IH(\mathbf{k})I^{-1} \neq H(-\mathbf{k})$ (with $I = \sigma_x K$, where K is complex conjugation), but time-reversal symmetry $\Theta H(\mathbf{k})\Theta^{-1} = H(-\mathbf{k})$ is preserved. This Hamiltonian exhibits 8 distinct Weyl nodes (see 6.1.1) divided in 4 nodes per k_y (due to introducing two non-zero k-momenta k_{x_0} and k_{z_0}) at

$\mathbf{K}_{WS_1} = (k_{x_0}, 0, k_{z_0})$, $\mathbf{K}_{WS_2} = (\pi - k_{x_0}, 0, k_{z_0})$, $\mathbf{K}_{WS_3} = (k_{x_0}, 0, \pi - k_{z_0})$ and $\mathbf{K}_{WS_4} = (\pi - k_{x_0}, 0, \pi - k_{z_0})$ as well as $\mathbf{K}_{WS'_1} = (k_{x_0}, \pi, k_{z_0})$, $\mathbf{K}_{WS'_2} = (\pi - k_{x_0}, \pi, k_{z_0})$, $\mathbf{K}_{WS'_3} = (k_{x_0}, \pi, \pi - k_{z_0})$ and $\mathbf{K}_{WS'_4} = (\pi - k_{x_0}, \pi, \pi - k_{z_0})$.

6.1.2 Model II: Breaking time-reversal symmetry

Similarly, breaking time-reversal symmetry yields the Hamiltonian:

$$H(\mathbf{k}) = \sum_{\mathbf{k}} \big[\epsilon_{\mathbf{k}} + (2t(\cos(k_x) - \cos(k_0)) + m(2 - \cos(k_y) - \cos(k_z)))\,\sigma_x + 2t\sin(k_y)\sigma_y + 2t\sin(k_z)\sigma_z\big] c^\dagger_{\mathbf{k}} c_{\mathbf{k}} + h.c. \tag{M2}$$

This model breaks time-reversal symmetry since $\Theta H(\mathbf{k})\Theta^{-1} \neq H(-\mathbf{k})$ but the inversion symmetry $I = \sigma_x K$ is preserved, where K represent complex conjugation. The model hosts 2, 6 or 8 Weyl nodes in the bulk Brillouin zone depending on the parameters m and k_0. This is explained in Appendix D. We focus on the regime where it only has 2 nodes, located on the Brillouin zone at $\mathbf{K}_{WS\pm} = \pm(k_0, 0, 0)$, related by inversion symmetry. Fixing k_x, $H_{k_x}(k_y, k_z)$ can be viewed as a 2D band structure, which is fully gapped when $k_x \neq k_0$ and its Chern number $\mathbb{C}_{k_x}$ is well defined. It can be easily shown that $\mathbb{C}_{k_x} = 1$ when $k_x \in (-k_0, k_0)$ and $\mathbb{C}_{k_x} = 0$ otherwise as can be seen in figure 6.1 [62].

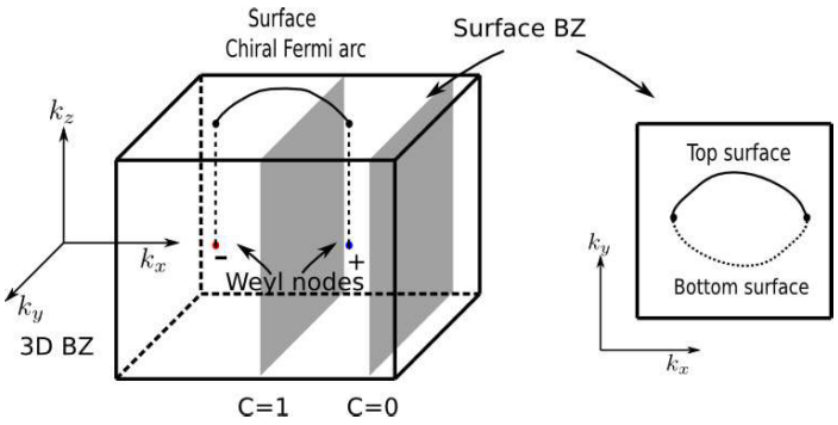

Figure 6.1: Weyl nodes in the two-band model II. The Chern number for the 2D band structure $\mathbb{C}_{k_x}$ at a given k_x is jumping by 1 across the nodes. As a result, there are surface chiral Fermi arcs. The arcs on the top and bottom surfaces form a closed 2D Fermi surface. From [63].

6.1.3 Incorporating the models on a lattice

The Hamiltonians of the models presented above both exhibit Weyl nodes at finite momenta $\mathbf{K}$. Since this is localized in momentum space, this is represented by a plane wave in position space according to the uncertainty principle. On the other hand, dislocations are naturally embedded within the crystal structure, and thus localised in position space. This duality in the relevant information about the system requires working in different settings, altering between the spaces. By making use of the translational symmetries of the Hamiltonian in one or two dimensions, we can make use of the periodicity in momentum space, and thereby making our system significantly bigger computationally.

In order to go from momentum space to position space, for the x-coordinate for example, it holds that, through Fourier transformation:

$$c_{\mathbf{k}} = \frac{1}{L}\sum_{j} e^{ik_x j} c_{k_x,j}.$$

Recall that

$$\sin(\alpha) = \frac{e^{i\alpha} - e^{-i\alpha}}{2i}, \qquad \cos(\alpha) = \frac{e^{i\alpha} + e^{-i\alpha}}{2i}.$$

Combining this results in the behaviour of the system in real space. This yields for model I:

$$H(\mathbf{r}) = \sum_{i,j} \big[-2(i + \sin(k_{x_0}))\sigma_x - 2i\sigma_y - 2(i + \sin(k_{z_0}))\sigma_z \big] c^{\dagger}_{\mathbf{r}_i} c_{\mathbf{r}_j} + h.c.$$

Further writing out the elements of the equation above yields the real-space site 'hopping' coefficient from site $\mathbf{r}_i$ to $\mathbf{r}_j$ and back (the $h.c.$ part). Having computed this, we can solve our Hamiltonian in real space. This gives a good perception of the distribution of energy modes and their localisation. In order to see this, consider the Hamiltonian of model I. We work in $1D$ spatial dimension for the y direction, and computing the band structure of the effective Hamiltonian $H(k_x, y, k_y)$ making use of the translational symmetry in the k_x and k_y direction yields the four zero Weyl nodes as can be seen in figure 6.2. Solving the same Hamiltonian in 2 spatial dimensions and using the translational symmetry in the k_z direction yields the energy band structure of figure 6.3.

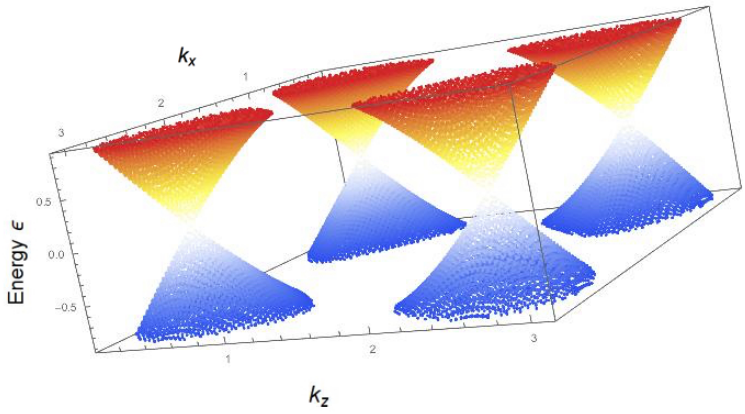

Figure 6.2: The energy band structure of a Weyl semimetal satisfying the Hamiltonian of model I. Here the energy ϵ is plotted as a function of the momenta k_x and k_z for the effective Hamiltonian $H(k_x, y, k_z)$ of model I. For this case, k_{x_0} and k_{z_0} have been set to $\frac{\pi}{6}$. The system exhibits four distinct Weyl nodes of zero energy at $\mathbf{K}_{y,WS_1} = (\frac{\pi}{6}, \frac{\pi}{6})$, $\mathbf{K}_{y,WS_2} = (\frac{\pi}{6}, \frac{5\pi}{6})$, $\mathbf{K}_{y,WS_3} = (\frac{5\pi}{6}, \frac{\pi}{6})$ and $\mathbf{K}_{y,WS_4} = (\frac{5\pi}{6}, \frac{5\pi}{6})$.

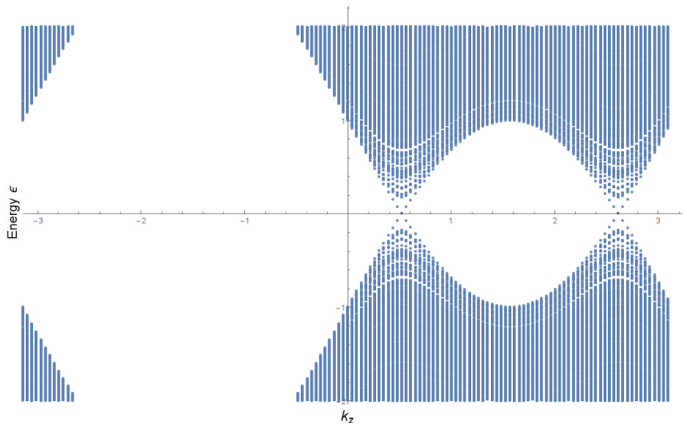

Figure 6.3: The energy band structure of a Weyl semimetal satisfying the Hamiltonian of model I. Here the energy ϵ is plotted as a function of the momentum k_z for the 2D effective Hamiltonian $H(x, y, k_z)$ of model I. The system exhibits two distinct Weyl nodes of zero energy at $\mathbf{K}_{xy,WS_1} = k_{z_0} = \frac{pi}{6}$ and $\mathbf{K}_{xy,WS_2} = \frac{5\pi}{6}$.

Once the interplay between the two spaces has been mastered, dislocation can be wired into the crystal structure in two or three spatial dimensions, yielding a dislocation vortex or a dislocation line, respectively. The effect of the position of the dislocation is studied through the application of the **K-b-t** rule in the next section.

6.2 Applying the K-b-t rule

The presence of a topological defect in the lattice structure engenders a change in the overall behaviour of the semimetal. Its effect is a notable result of the interplay between geometry and topology. This effect however depends on the position of the defect. This is reflected by the **K-b-t** rule. In the models studied, the momenta $\mathbf{K}_{WS_i}, (i = 1, 2, 3, 4)$ for model I and $\mathbf{K}_{WS_j}, (j = +, -)$ for model II are taken to have finite k_x, k_z and k_x, respectively, while $k_y = 0$ for both cases. According to the **K-b-t** rule, only dislocations that are perpendicular to the direction of $\mathbf{K}$ will unveil dislocation modes. This can be appreciated when studying the model in 3 spatial dimensions as can be seen in the figures 6.4, 6.6 and 6.5. To start with, the normal energy band structure as a function of the number of modes is computed for model I.

Figure 6.4 shows the dispersion relation of the model when the crystal lattice is dislocation-free. As computed, it exhibits zero modes as can be seen in the figure.

For a dislocation along the x-direction, the Burgers vector equals $\mathbf{b} = be_{\mathbf{y}}$. According to the **K-b-t** rule, this yields an additional flux $\mathbf{\Phi} = \mathbf{K} \cdot \mathbf{b} = 0$ for $\mathbf{K}_{WS_i}$. Therefore no extra dislocation modes can be seen at low energy as pictured in figure 6.5.

For a dislocation along the y-direction, the Burgers vector equals

$\mathbf{b} = be_{\mathbf{x}}$. This yields an additional flux $\mathbf{\Phi} = \mathbf{K} \cdot \mathbf{b} = \pm k_0 \cdot b$ which leads to dislocation modes in the band structure as seen in figure 6.6. Hence, the dependence of the effect of the dislocations on the topology of the crystal is clear as well as the dependence of the change in the behaviour of the semimetal on the geometry of the dislocations.

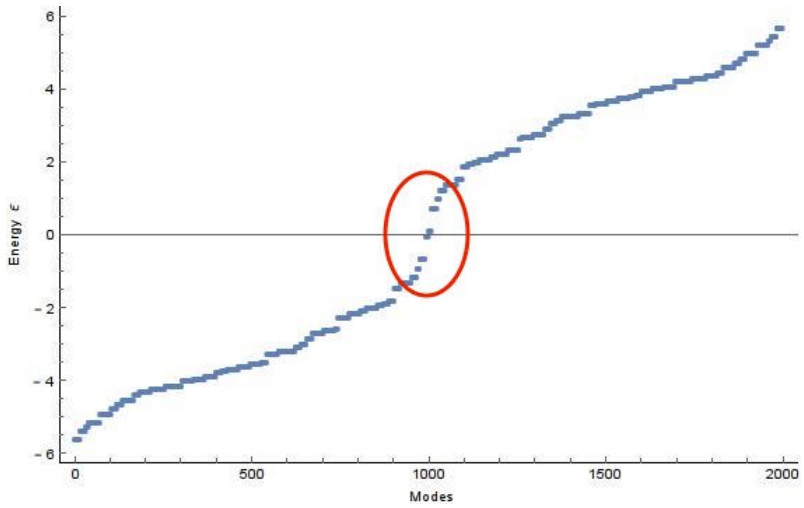

Figure 6.4: Energy band structure of model I with no present dislocations as a function of the number of modes. Each blue point represent a distinct energy mode. The red ellipse encloses the energy band width containing low energy modes, which the part of interest and represent the behaviour of the low energy effective Hamiltonian around the Weyl nodes.

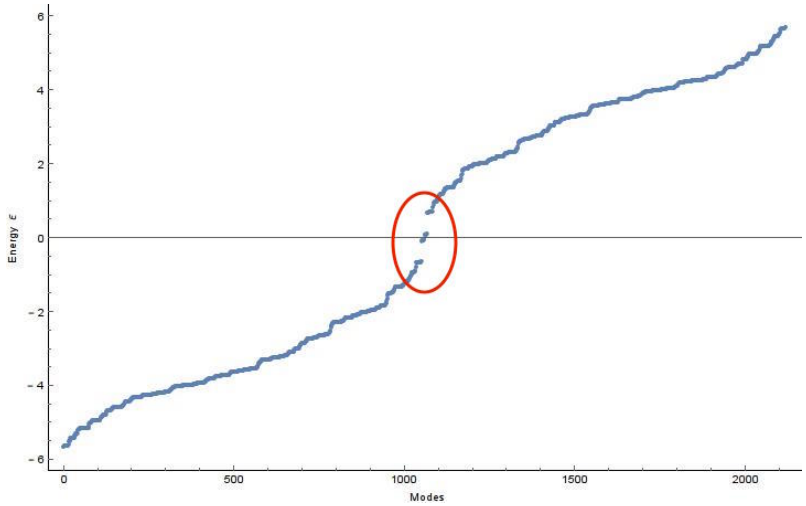

Figure 6.5: Energy band structure of model I with a dislocation along the x-direction. Here, the Burgers vector equals $\mathbf{b} = be_{\mathbf{y}}$. The **K-b-t** rule yields no effect of the dislocation on the band structure at low energy as can seen within the red ellipse.

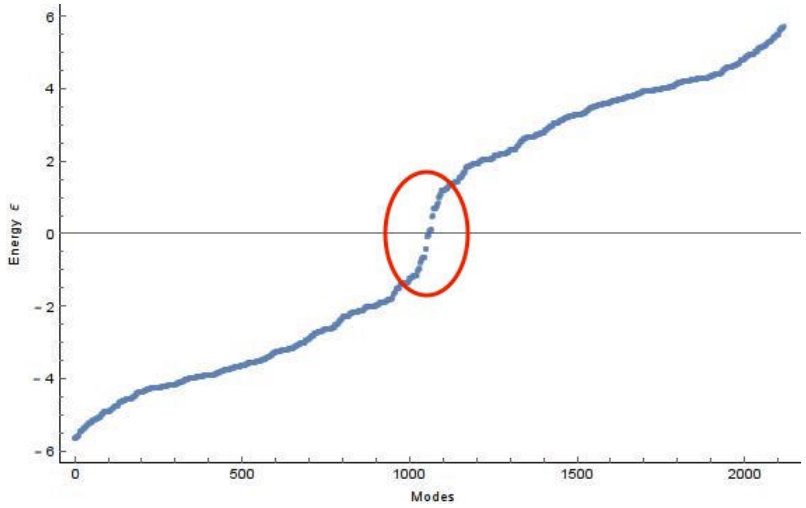

Figure 6.6: Energy band structure of model I with a dislocation along the y-direction. Here, the Burgers vector equals $\mathbf{b} = be_{\mathbf{x}}$. The **K-b-t** rule yields a multiplication of the wavefunctions by a phase factor $\phi = k_0 \cdot b$. This results in the creation of additional dislocation modes at low energy as can seen within the red ellipse.

Accordingly, the next computations were solely based on dislocation lines along the y-direction, which yield a Burgers vector $\mathbf{b} = be_{\mathbf{x}}$.
The effect of a dislocation can be seen in figure 6.6 where the energy band gap "fills up" and new states appear to "come down" in energy. This suggests the possible presence of zero energy dislocation modes, that would allow for transport possibilities between the Weyl nodes.
In order to do this, we study the response of the Weyl semimetals using the relation

$$H_{3D}(x, y, z) = \sum_{k_z} e^{ik_z z} H^{2D}_{\text{eff}}(x, y, k_z).$$

for a dislocation along the y-direction on a 2D roster while making use of the translational symmetry in the k_z direction. The energy band structures computed for perfect crystal as well as the "perturbed" crystal (where a dislocation is present) are presented in figures 6.7 and 6.8.

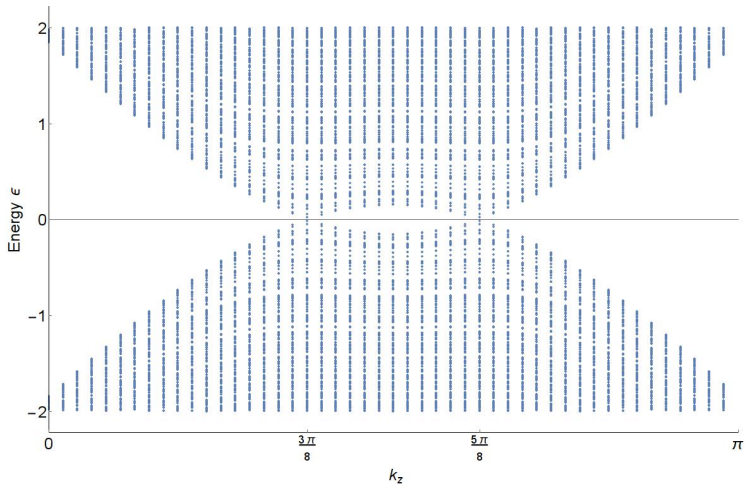

Figure 6.7: Energy band structure for the Weyl semimetal of model I for $k_0 = \frac{3\pi}{8}$ when no dislocation is present on a 60×60 sized roster. The band structure is gapless at two Weyl nodes for $k_z = \frac{3\pi}{8}, \frac{5\pi}{8}$. The plot range is limited to $k_z \in [0, \pi)$ since both Weyl nodes are localised within this range.

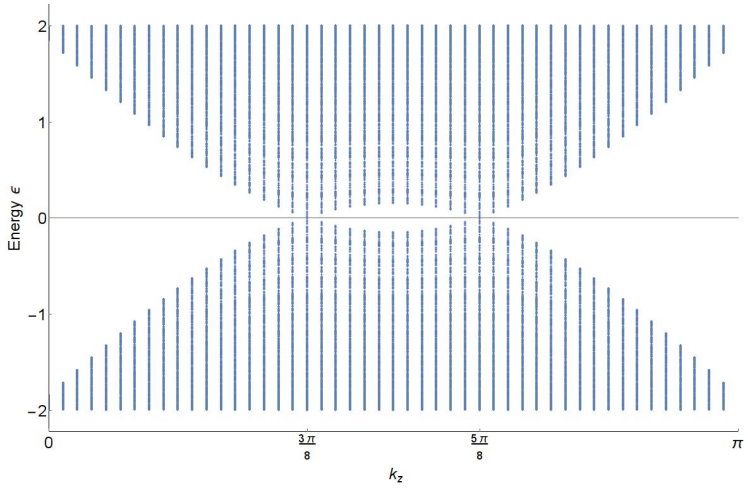

Figure 6.8: Energy band structure for the Weyl semimetal of model I for $k_0 = \frac{3\pi}{8}$ in the presence of a dislocation in the y-direction on a 60×60 sized roster. The plot range is limited to $k_z \in [0, \Pi)$ since both Weyl nodes are localised within this range at $k_z = \frac{3\pi}{8}, \frac{5\pi}{8}$. The dislocation leads to the additional creation of dislocation modes as can be seen compared to figure 6.7.

The difference in the electronic band structure with the presence of a dislocation in a specific direction raises the question whether (zero energy) dislocation modes appear within the band structure that would facilitate transport, or "pumping" between the chiral nodes.

6.3 The search for zero energy dislocation modes

Although it has been demonstrated that 3D topological insulators support propagating helical modes, due to the presence of a dislocation aligned along the Burgers vector along the direction of a non-Γ band inversion point [54], this is not trivial in the case of Weyl semimetals, as

we have a semimetal and not an insulator. This means that the addition of a dislocation along the direction of a non-trivial Weyl node results in the additional creation of states in the bulk that might be absorbed in the bulk. Another difference is the presence of multiple cones, instead of a single one. This complicates the search for zero energy dislocation modes, as presented in the next section.

6.3.1 Zero energy dislocation modes for model I

The effectuated computations have mainly been done for model I, since here the Weyl nodes are situated at finite k_z and thus, wiring in a dislocation line in the z-direction has a non-trivial effect, as elucidated by the **K-b-t** rule.

Dislocation modes

Distinguishing between the energy of the bulk modes and the dislocation modes can be a tough task. A dislocation mode is characterised by a localisation around the dislocation line (or vortex in case of a 2D system) of its corresponding eigenvector as can be seen in figure 6.9. Therefore, the distinction is done by extracting the relevant modes satisfying this. The overall energy band structure of the bulk and dislocation modes can be seen in figure 6.10 and the filtered energy band structure of the sole dislocation modes in figure 6.11.

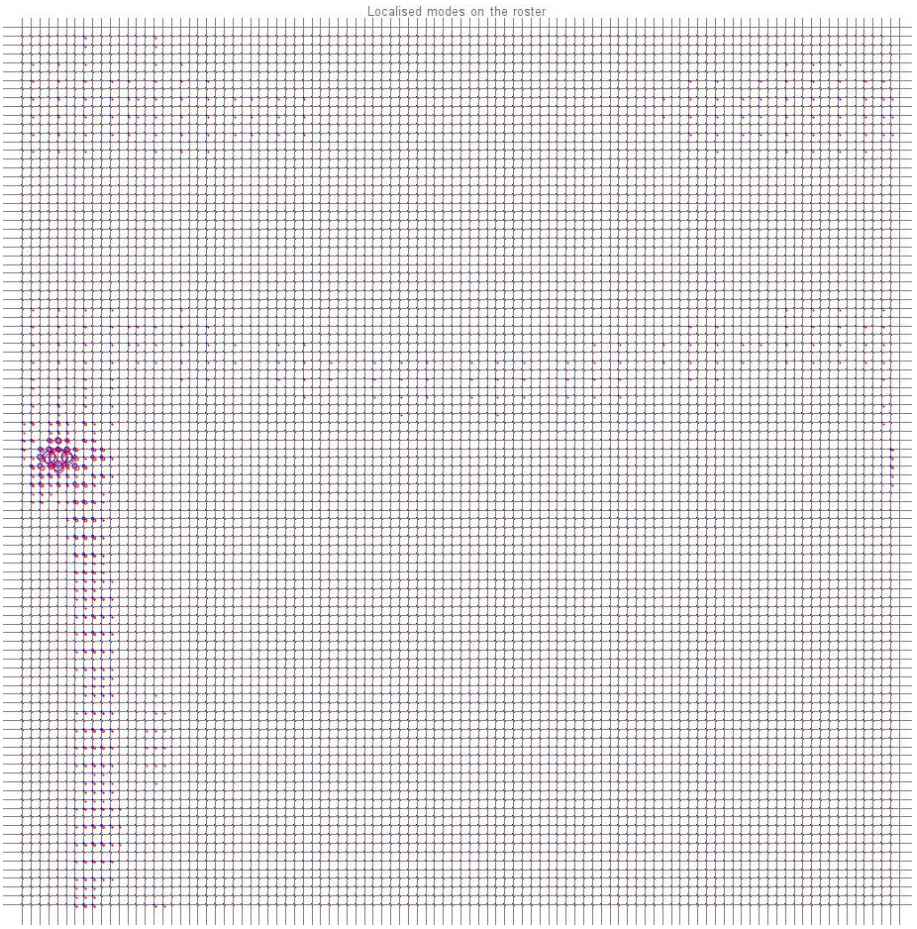

Figure 6.9: Localised dislocation modes on the real space roster of atoms of size 100×100 . The blue and red circles represent the weight of the eigenvector at a given spatial coordinate (x_i, y_i) and represent different spin. In this case, the dislocation has been introduced between $x_i = 5$ and $x_i + 1 = 6$ and goes along the y_i-direction up to $y = 100/2 + 1 = 51$, where the eigenvector is clearly localised.

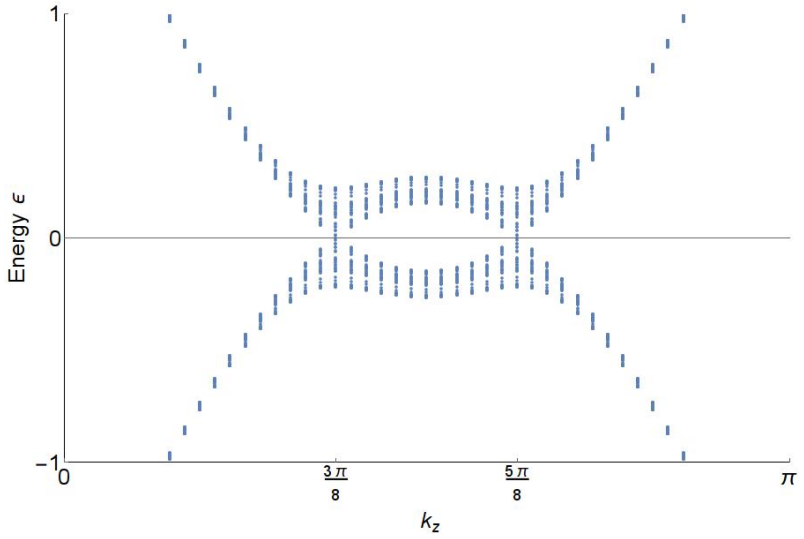

Figure 6.10: Energy band structure for model I for $k_0 = \frac{3\pi}{8}$ in the presence of a dislocation. The energies are limited to the smallest 80 values for each k_z.

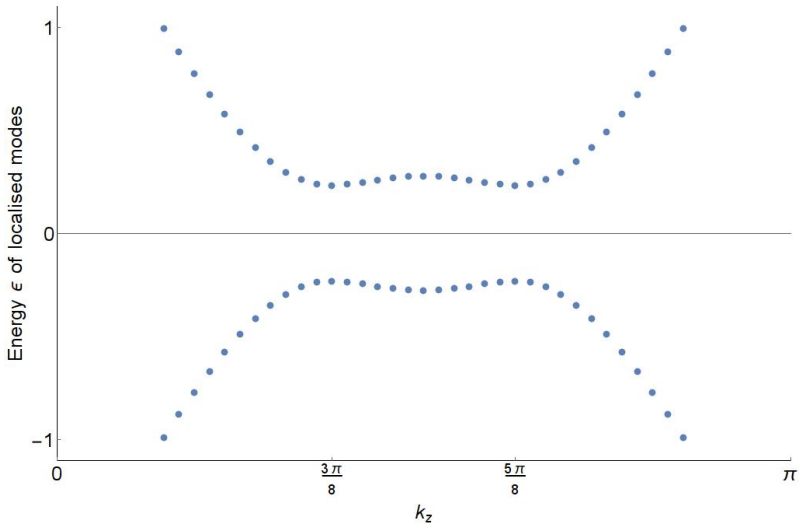

Figure 6.11: Energy dispersion of the localized dislocation modes as a function of the value of k_z in the presence of a dislocation in the y-direction. For each k_z, there are two localised dislocation modes. The system is is gapless in the bulk for $k_0 = \frac{3\pi}{8}, \frac{5\pi}{8}$ but clearly the energy gap between the localised modes is finite (and minimal for both Weyl nodes)

The numerical simulations presented in figure 6.11 reveal that model I does not allow for the creation of zero energy dislocation modes. Although te system is gapless in the bulk (figure **??**) , the energy of the localised dislocation modes is finite, for each distinct k_z. In order to study and simulate the response of the Weyl semimetal from a different perspective, we introduce a π-flux vortex, which mimics the behaviour of a spatial dislocation.

π-flux

As the the response of the model I Weyl semimetal upon introducing a dislocation did not yield any zero energy dislocation modes, its behaviour is studied upon introducing a π-flux vortex, which itself mimics the effect of a lattice dislocation. A π-flux is created by making use of anti-periodic boundary conditions between two adjoining lattice sites (x_i, y_i) and (x_{i+1}, y_i), by multiplying the hopping coefficient with a phase $e^{-i\pi}$ when hopping from site (x_{i+1}, y_i) to site (x_i, y_i) (and by a phase $e^{i\pi}$ when hopping the other way around). The energy band structure of the response model to this alteration is plotted in figure 6.12.

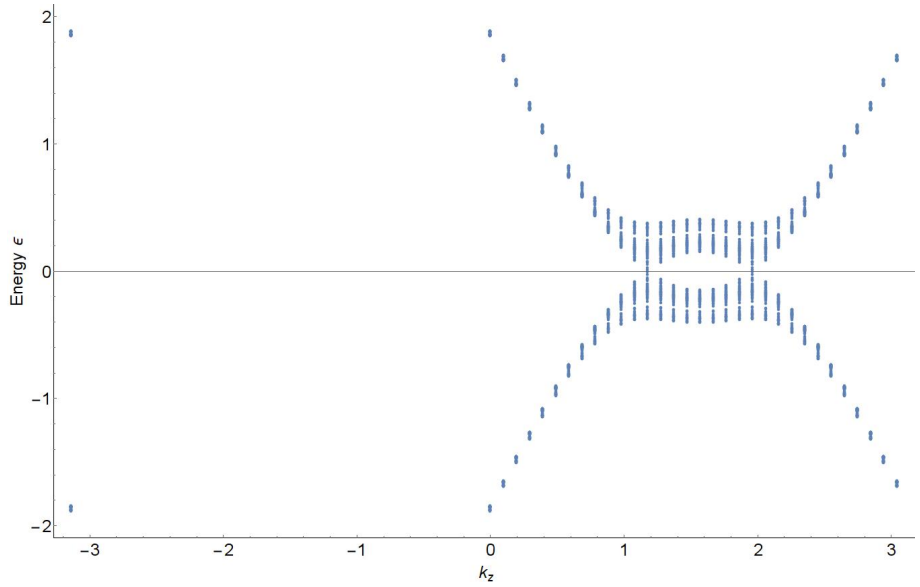

Figure 6.12: Energy band structure for model I for $k_0 = \frac{3\pi}{8}$ in the presence of a π-flux. The energies are limited to the smallest 80 values for each k_z.

Following the same procedure as with a dislocation line for a *pi*-flux vortex along the y-direction, π-flux modes with an eigenvector localised around the vortex core of the π-flux are identified.
This yields the energy band structure for the localised π-flux modes of figure 6.13.

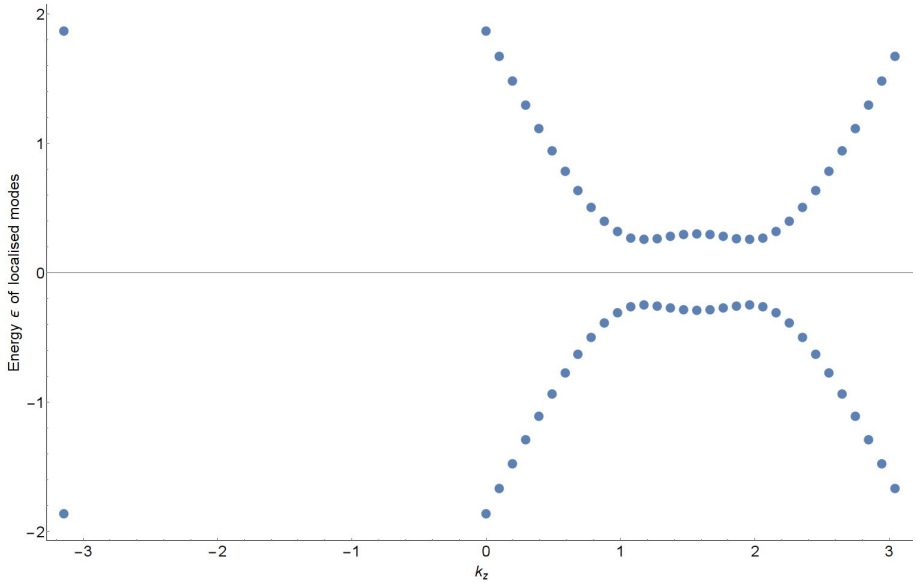

Figure 6.13: Energy dispersion of the localized dislocation modes as a function of the value of k_z in the presence of a π-flux in the roster. For each k_z, there are two localised dislocation modes. The system is is gapless in the bulk for $k_0 = \frac{3\pi}{8}, \frac{5\pi}{8}$ but clearly the energy gap between the localised modes is finite (and minimal for both Weyl nodes).

Here again, the presence of the π-flux vortex does not yield any zero energy vortex modes as the energy band gap is clearly finite for each k_z in figure 6.13. This is different from the response that is found for the case of a topological band insulator. Remember that the latter only exhibits one cone. Hence, would the presence of 4 Weyl nodes alter the creation of zero energy vortex modes? In order to find an adequate explanation and a correlation for this, the change in the finiteness of the energy band gap between vortex modes as a function of the value of k_0 is studied.

Dependence of the dislocation mode energy band gap on k_0 for model I

Model I exhibits dislocation modes at finite energy. Therefore there are no extra zero helical dislocation modes upon the addition of a dislocation to the lattice of the crystal and no transport is possible between the nodes. This is contrary to what was found when a dislocation was embedded in a TBI, as done in [54]. Model I displays 4 distinct Weyl nodes, of different chiralities. This result raises the question on how this finite energy depends on the distance between the Weyl nodes, which is given by $\Delta_{WN} = 2k_0$ and their possible interaction, that would "gap" the dislocation modes.

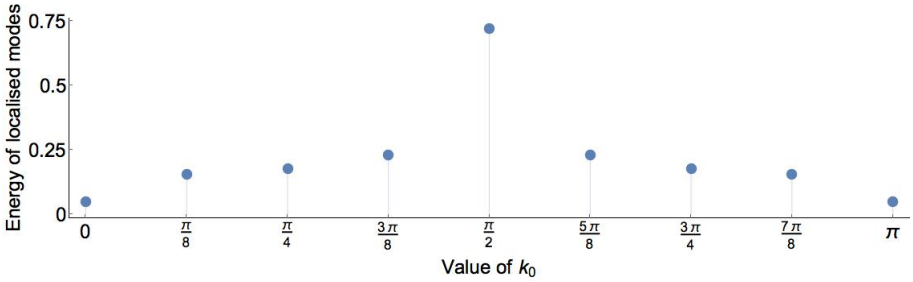

Figure 6.14: Energy dispersion of the dislocation modes (DM) for model I when computed for a 50×50 roster of atoms as a function of the node splitting value k_0. Clearly, there is a correlation between the distance between the Weyl nodes, which is equal to $\Delta_{WN} = 2k_0 \mod \pi$. This distance is minimized for $k_0 = \frac{\pi}{2}$ and at this distance yields a maximal finite energy for the dislocation mode equal to 0.72. When the distance is set to $k_0 = \frac{\pi}{8} \mod \pi$, the energy of the dislocation mode equals 0.15. Note that, for the case, $k_0 = 0 \mod \pi$, where we have pairs of Weyl nodes, the energy band gap is found to equal to be 0.05.

Thus, the search for zero energy dislocation dislocation and *pi*-flux vortex modes revealed that some additional mechanism comes into play and

changes the game, compared to the case of a TBI. Since there seems to be a correlation between the distance between the Weyl nodes, model II is studied, as it only displays 2 Weyl nodes and it breaks a different symmetry. This is done in the next section.

6.3.2 Zero energy dislocation modes for model II

Model II breaks time-reversal symmetry, unlike model I. It possesses two Weyl nodes at $\mathbf{K}_{WS_\pm} = (\pm k_0, 0, 0)$. The presence of Weyl nodes at $k_z = 0$ renders the study of the model, using translational symmetry in the z-direction, as a function of the value k_z irrelevant since both Weyl nodes are projected onto the $k_z = 0$ plane. Thus we study the behaviour of the system in the case of a two dimensional spatial roster by looking at the energy band structure as a function of the number of modes present. The effective two dimensional Hamiltonian is then given by

$$H(k_x, k_y) = \sum_{\mathbf{k}} \left[(2t(\cos(k_x) - \cos(k_0)) + m(1 - \cos(k_y)))\sigma_x - 2t\sin(k_y)\sigma_y\right] c^\dagger_{\mathbf{k}} c_{\mathbf{k}} + h.c.$$

Setting $t = 1, k_0 = \frac{3\pi}{8}$ and $m = \frac{3}{2}$, this model exhibits two Weyl nodes of zero energy at $K_{2D,WS_\pm} = (\pm k_0, 0)$.
Following the outline of the study of model I, both cases of a dislocation and a π-flux vortex are studied.

Dislocation modes

The search for zero energy dislocation modes for the case of model II is similar to the one for model I. Here, the change in the overall energy band structure as a function of the number of modes is analysed. The

overall energy band structure of the Weyl semimetal when no dislocation is present is plotted in figure 6.15. Here, we have to account for the numerical error (We are obliged to used the numerical value of $\cos(\frac{3\pi}{8})$) and the finite size effect, yielding a deviation of the zero energy of $\varepsilon = \pm 0.02$. The effect of a dislocation along the y-direction on the energy band structure is presented in figure 6.17. Clearly, there is a change in the low energy behaviour of the semimetal and new modes seem to have been created.

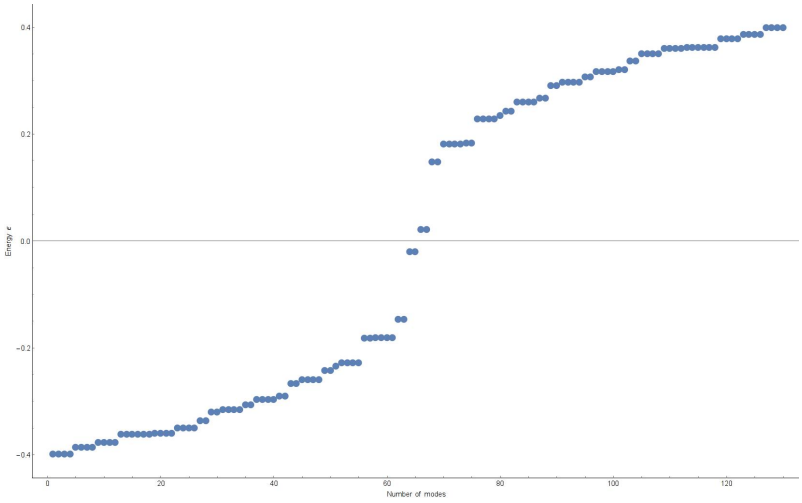

Figure 6.15: Energy band structure of model II (zoomed in) when a dislocation is present along the y-direction on a 70×70 sized roster and making use of the translational symmetry in the k_z direction. Accounting for numerical deviations (The numerical value of $\cos\frac{3\pi}{8}i$ used) and for finite size effect, the model allows for zero energy modes.

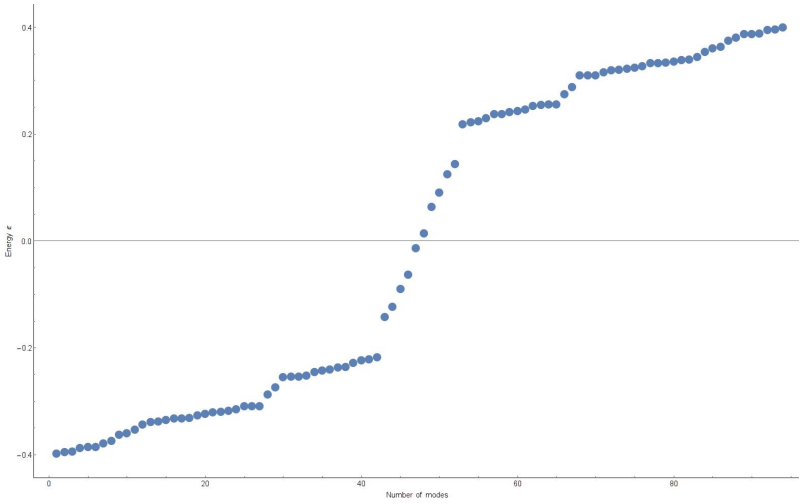

Figure 6.16: Energy band structure of model II (zoomed in) when a dislocation is present along the y-direction on a 70×70 sized roster and making use of the translational symmetry in the k_z direction. Accounting for numerical deviations (The numerical value of $\cos \frac{3\pi}{8} i$ used) and for finite size effect, the model allows for zero energy modes.

Filtering out the localised dislocation modes as has been done before, we are left with two localised modes as can be seen in figure 6.17. Taking into account the numerical errors, the presence of a dislocation thus yields two localised zero energy dislocation modes.
Following this resultm it is interesting is to see whether the same result is obtained with the presence of a π-flux vortex, and whether the numerical error can be optimized.

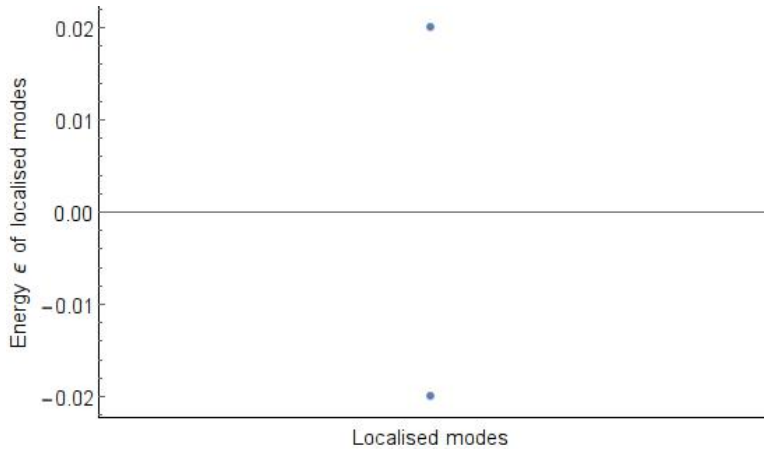

Figure 6.17: Energy of the localised dislocation modes. The energy of the localised modes is equal to ± 0.02, which can be still accounted for as a finite size and numerical error effects. Only two dislocation modes are found at this energy

π-flux

Introducing a π-flux vortex along the y-direction for the two dimensional version of model II gives the energy band structure of

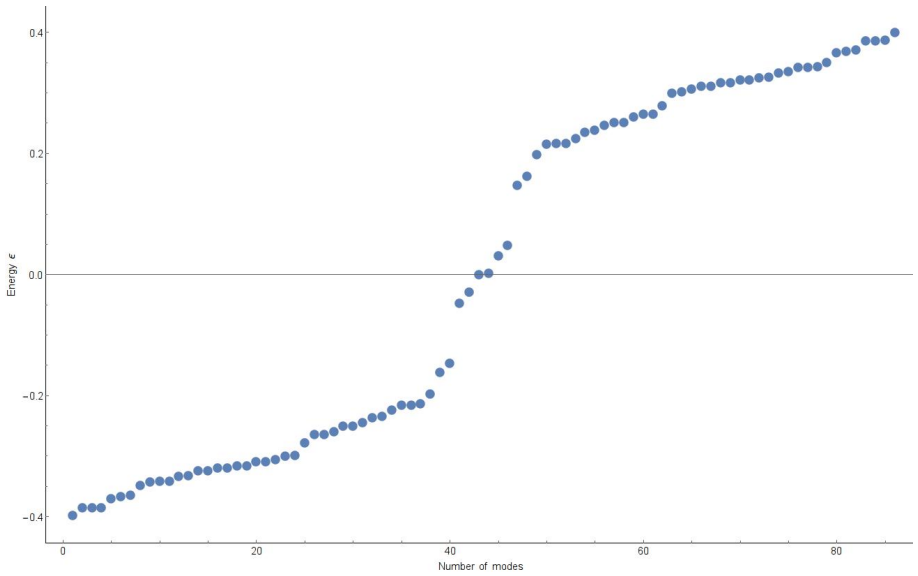

Figure 6.18: Energy band structure of model II (zoomed in) in the presence of a π-flux as a function of the number of modes on a 60×60 sized roster. The model clearly allows for two zero modes.

Filtering out the localised dislocation modes yields an eigenvector localised around the π-flux vortex as seen in figure 6.19.

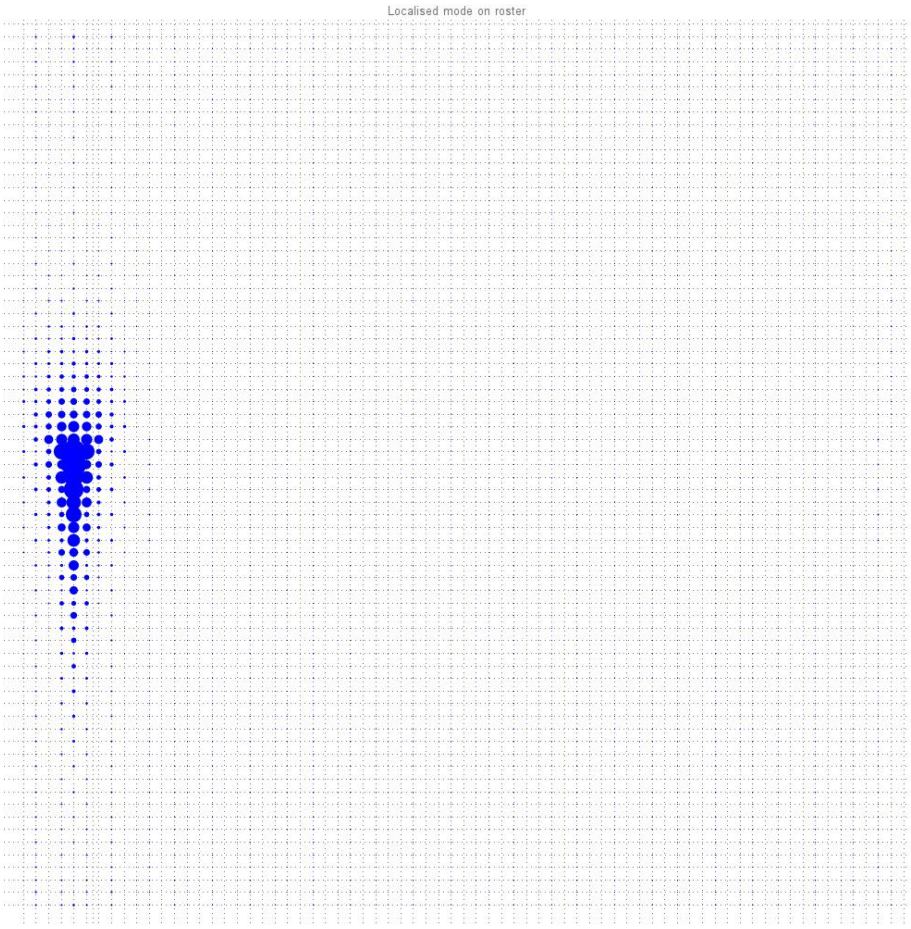

Figure 6.19: Localised π-flux modes on the real space roster of atoms. The blue disks represent the weight of the eigenvector at a given spatial coordinate (x_i, y_i) and represent different spin. In this case, the π-flux has been introduced between $x_i = 5$ and $x_i + 1 = 6$ and goes along the y_i-direction up to $y = 70/2 + 1 = 36$, where the eigenvector is clearly localised.

This results in two localised π-flux vortex modes as plotted in figure 6.20. The modes have an energy of ± 0.000981951. Accounting for the finiteness of the roster, these localised modes count as zero energy π-flux vortex modes.

Figure 6.20: Energy of the localised π-flux modes. The energy of the localised modes equals ± 0.000981951, which is accounted for a finiteness size numerical error. Here again, only two dislocation modes are found at this energy.

Since the effect of a dislocation and π-flux on the energy band structure of model II have only been studied in the $k_z = 0$ plane, the dependence of the former on the value of k_z constitutes a valid question and is elucidated in the next section,

Dependence of the dislocation mode energy band gap on k_z for model II

The presence of zero energy modes for model II as studied for a 60×60 sized roster in the $k_z = 0$ plane raises the question whether this is unique for this slice, and how this dislocation energy band depends on the k_z-"slice" taken. Figure 6.21 clearly demonstrate a correlation between the value of K_z and the finiteness of the energy of the localised modes. This is analysed in the next section.

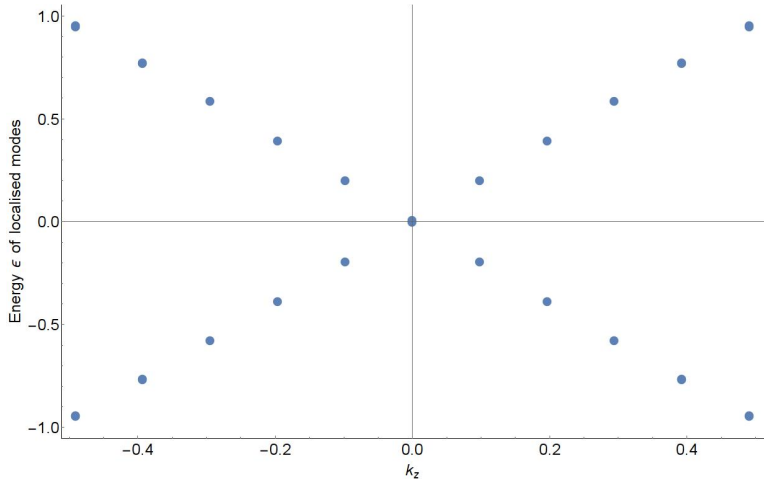

Figure 6.21: Energy gap of the localised modes as a function of k_z for model II. The system only allows for zero energy dislocation modes for $k_z = 0$. For any other value of k_z, the dislocation modes reside at finite energy. A linear relation between the value of k_z and the width of the energy band gap is evident.

6.4 Discussion

The effect of a dislocation and a π-flux line (vortex) in the case of two 3D (2D slice of a 3D) dimensional Weyl semimetals has been studied for the possibility of transport between Weyl nodes. Model I, which breaks inversion symmetry bur preserves time-reversal symmetry clearly does not allow for the creation of zero energy dislocation or π-flux modes. Model II, which breaks time-reversal symmetry but respects inversion symmetry, seems to allow for the presence of the latter for the unique value of $k_z = 0$.

Breaking different symmetries, as discussed in chapter 2, yields a different amount of Weyl nodes as well as different related chiralities. On the one hand, model I exhibits 4 Weyl nodes, given by two pairs of Weyl

nodes with of same chirality at $\pm\mathbf{k}_0$ and $\mathbf{k}_0'$. This has been established by Young and Kane in [64]. Recall that time-reversal symmetry imposes that if a Weyl node present at momentum $\mathbf{k}_0$, another Weyl node of same chirality is present at momentum -$\mathbf{k}_0$. Since the total chiral number of the Fermi surface has to vanish, this requires the additional existence of two Weyl nodes of opposite chirality at momenta $\pm\mathbf{k}_0'$. As established, the distance between the Weyl nodes plays a significant role in the width of the finite energy band gap between the localised dislocation modes. A minimal distance of $k_0 = \frac{\pi}{2}$ engenders an energy of ± 0.7 for the dislocation modes. We found that the energy gap diminishes for growing distance. This suggest that the Weyl nodes tend to want to hybridise and that the interaction between the former prevents the system from creating zero energy dislocation modes.

On the other hand, model II exhibits 2 Weyl nodes of opposite chirality. As established, this model allows for the creation of zero energy dislocation modes, unlike model I. Since this model respects inversion symmetry, each mode of positive energy has a counterpart of negative energy. This means that the zero energy dislocation modes can in principle be "gapped out" by introducing a perturbation, where the energy of the dislocation mode corresponding to the +1 (-1) Weyl node would be finite and positive (negative) without breaking inversion symmetry. This can be done because of the existence of two Weyl nodes. In the case of a single Weyl node, this would not be possible, since it is topologically protected by inversion symmetry.

The presence of an even number of Weyl nodes for each k_x-k_y-plane for both models suggests that the dislocation modes, whether at finite or zero energy, are not topologically protected and can be "moved" around or gapped out. Therefore, no chiral "pumping" can be done between

the Weyl nodes.

This brings up the question whether this pumping can be done in the presence of a dislocation line in case of single in-plane Weyl node since a zero energy dislocation mode would be topologically protected. This can be done by means of a screw dislocation along the xy-plane, which would give a dislocation line in the z-direction accompanied by a Burgers vector in the z-direction. In the case of an inversion symmetry preserving model with non-zero k_z, this would have a single zero dislocation mode for each non-zero k_z. These would then be protected by inversion symmetry and chiral pumping may occur between the Weyl nodes. However, this prediction can to be further worked out building on the work done in this thesis with the adequate simulations.

Chapter 7

Conclusions and outlook

In conclusion, this thesis studied the structure and the topology of Weyl semimetals and presented their recent discoveries in realistic materials. Building on this knowledge, the response of two types of Weyl semimetals has been studied upon the introduction of a dislocation line or a pseudo-magnetic π-flux. Basically, a lattice dislocation imposes a phase shift on the wave functions, which, following the **K-b-t** rule, is equal to the inner product of the Burgers vector **b** and the momentum of the Weyl node wave function **K**. As a result, only wave functions with finite momentum in the direction of the Burgers vector are affected by the dislocation or π-flux. In the continuum approximation, the effect of the topological defects only attains a finite value if the Weyl cone expanded around is located at finite momentum **K**. Particularly, this occurs when $\mathbf{K} \cdot \mathbf{b} \neq 0 \mod 2\pi$.

In addition to the **K-b-t** rule for dislocations (and π-fluxes), the breaking of different symmetries, time-reversal symmetry and inversion symmetry, has led to a distinct behaviour when it comes to the presence of zero energy dislocation modes of which the explicit form given by the

eigenvectors reveals that they are exponentially localized at the vortex core.

The presence of multiple pairs of Weyl nodes of same chirality engendered by the breaking of inversion symmetry has been found to prevent the creation of zero energy dislocation modes. The Weyl nodes are suspected to be interacting and therefore"hybridising" the dislocation modes. The correlation between the distance of the Weyl nodes in momentum space and the width of this finite energy gapping has been established numerically. The breaking of time-reversal symmetry in a $m - B$ model (model II) unveils a pair of Weyl modes of opposite chirality. The introduction of a dislocation or a π-flux has been found to allow the creation of zero energy dislocation modes. Since this is protected by inversion symmetry, a simple perturbation would "gap" out these dislocation modes without breaking the former. We suspect that a zero energy dislocation modes would only be topologically protected in the case of the presence of a single Weyl node along the dislocation line at distinct k_z. This is realised with wiring in a screw dislocation. Thus, it is clear that the creation of zero energy dislocation modes depends on the topology of the Weyl semimetal, and on what symmetries are broken. The different parameters of the Weyl semimetal as well as the number and the chirality of the Weyl nodes are found to play an important for the existence of the zero energy modes. These findings bring into doubt the results of [65], since more factors have to be accounted for.

Although our results constitute a preliminary basis for the topological classification of the response of different Weyl semimetals to topological defects, further calculations can be done, accompanied with the adequate simulations, in order to confirm the predictions formulated and study the possibility of chiral pumping between chiral Weyl nodes.

Appendix A

Manifolds and vector bundles

Definition (Coordinate system, Chart, Parametrisation) Let $\mathcal{M}$ be a topological space and $\mathcal{U} \subseteq \mathcal{M}$ an open set. Let $\mathcal{V} \subseteq \mathbb{R}^n$ be open. A homeomorphism $\phi : \mathcal{U} \to \mathcal{V},\ \phi(u) = (x_1(u), \ldots, x_n(u))$ is called a coordinate system on $\mathcal{U}$, and the functions $x_1, \ldots x_n$ the coordinate functions. The pair $(\mathcal{U}, \phi)$ is called a chart on $\mathcal{M}$. The inverse map ϕ^{-1} is a parametrisation of $\mathcal{U}$.

Definition (Atlas, Transition maps) An atlas on $\mathcal{M}$ is a collection of charts $\{\mathcal{U}_\alpha, \phi_\alpha\}$ such that $\mathcal{U}_\alpha$ cover$\mathcal{M}$. The homeomorphisms $\phi_\beta \circ \phi_\alpha^{-1} : \phi_\alpha(\mathcal{U}_\alpha \cap \mathcal{U}_\beta) \to \phi_\beta(\mathcal{U}_\alpha \cap \mathcal{U}_\beta)$ are the transition maps or coordinate transformations.

A topological space is called second countable if the topology has a countable base, and Hausdorff if distinct points can be separated by neighbourhoods. A sketch of the transformations is given in Figure A.1.

Definition (Topological manifold, Smooth manifold) A second countable, Hausdorff topological space $\mathcal{M}$ is an n-dimensional topological manifold if it admits an atlas $\{\mathcal{U}_\alpha, \phi_\alpha\}, \phi_\alpha : U_\alpha \to \mathbb{R}^n,\ n \in \mathbb{N}$. It is

a smooth manifold if all transition maps are C^∞ diffeomorphisms, that is, all partial derivatives exist and are continuous.

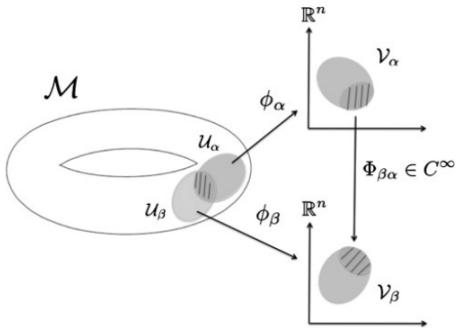

Figure A.1: A diagram of a smooth manifold and two compatible charts.

Definition A principal bundle with fibre F is a map $p : E \to X$ with the property that any point $x \in X$ has a neighbourhood $U \subseteq X$ for which there exists a homeomorphism $\phi_U : F \times U \to p^{-1}(U)$ for which $(p \circ \Phi_U) = \pi_2$ where π_2 is the projection $F \times X \to X$.

Appendix B

Discrete symmetries and Kramer's theorem

One of the most useful techniques to extract properties of a physical system is to exploit the various symmetries exhibited by the system. In quantum mechanics symmetries are represented by unitary and anti-unitary operators as follows from Wigner's theorem [69].The Wigner unitary-anti-unitary theorem on the representation of symmetry operations in quantum mechanics is an important result belonging to the mathematical foundations of the subject. The dominant role of unitary group representations in quantum physics can be traced to this theorem which states that any (invertible) map of the space of pure states (unit rays) of a quantum system onto itself preserving transition probabilities is induced by either a linear unitary transformation or an antilinear antiunitary transformation at the level of vectors in the complex Hilbert space pertaining to the system. That is, invariance of all transition probabilities demands that all probability amplitudes be either preserved or complex conjugated uniformly [70].

Theorem. *Let $\mathcal{H}$ be a complex Hilbert space and $\mathcal{T} : \mathcal{H} \to \mathcal{H}$ an arbitrary function. Then*

$$|\langle \mathcal{T}x, \mathcal{T}y \rangle| = |\langle x, y \rangle|$$

holds for any $x, y \in \mathcal{H}$ if and only if there exists a function $\phi : \mathcal{H} \to \mathbb{C}$ with $|\phi| = 1$ and a linear unitary or antilinear antiunitary isometry $U : \mathcal{H} \to \mathcal{H}$ such that $\mathcal{T} = \phi \cdot U$.

An operator A is called anti-unitary, if it maps the whole Hilbert space $\mathcal{H}$ onto itself, preserves the norm and fulfils $A(\alpha\psi+\beta\phi) = \alpha^*(A\phi)+\beta^*(A\psi)$ and $\langle A\phi|A\psi\rangle = \langle\phi|\psi\rangle^* = \langle\psi|\phi\rangle$. It is then obvious that an anti-unitary A operator can be represented by $A = UK$, with K as the complex conjugation operator that squares to unity and U a unitary operator. An important example is the time-reversal operator Θ. Time reversal amounts to

$$X' = X \quad P' = -P \quad \sigma' = -\sigma \quad S' = S$$

where the accent indicates the time reversed operators. Applying Θ on the commutator of the position and momentum operator yields

$$\begin{aligned}
\Theta i\hbar\Theta^{-1} &= \Theta[X, P]\Theta^{-1} \\
&= (\theta X\Theta)(\Theta^{-1}P\Theta^{-1}) - (\theta P\Theta)(\Theta^{-1}X\Theta^{-1}) \\
&= X'P' - P'X' \\
&= -(XP - PX) \\
&= -i\hbar
\end{aligned}$$

Henceforth Θ cannot be unitary and must therefore be antiunitary. Moreover, the above equation results in the following condition on a time reversal invariant Hamiltonian

$$\Theta H(\mathbf{k}, \mathbf{r})\Theta^{-1} = H(-\mathbf{k}, \mathbf{r})$$

We can now readily find the explicit form of the unitary part of the time reversal symmetry operator Θ for electrons. The complex conjugation operator reverses the momentum, whereas for the spin we get

$$\Theta|\uparrow\rangle = UK|\uparrow\rangle = |\downarrow\rangle$$

Adopting spherical coordinates yields

$$|\uparrow\rangle = \begin{pmatrix} \cos(\frac{\theta}{2}) \\ e^{i\phi}\sin(\frac{\theta}{2}) \end{pmatrix} \qquad |\downarrow\rangle = \begin{pmatrix} e^{-i\phi}\sin(\frac{\theta}{2}) \\ \cos(\frac{\theta}{2}) \end{pmatrix}$$

then leads to the conclusion that $\Theta = e^{\frac{i\pi\sigma_y}{\hbar}}$. Hence, the unitary part U equals $i\sigma_y$.

We observe that Θ squares to minus unity. This gives rise to what is known as Kramers theorem (see Section B.1). Likewise, inversion symmetry and chiral symmetry can be evaluated in exactly the same manner. The result is that inversion symmetry is represented by a unitary matrix I with corresponding expression

$$IH(\mathbf{k},\mathbf{r})I^{-1} = H(-\mathbf{k},-\mathbf{r})$$

whereas chiral symmetry is expressed by means of a unitary operator Π satisfying

$$\Pi H(\mathbf{k},\mathbf{r})\Pi^{-1} = -H(-\mathbf{k},\mathbf{r})$$

B.1 Kramer's Theorem

Theorem. *If for an operator $\mathcal{T}$ it holds that $\mathcal{T}^2 = -1$, then $\mathcal{T}|\psi\rangle$ yields a quantum state different from $|\psi\rangle$.*

Proof. Assume $\mathcal{T}|\psi\rangle = e^{i\phi}|\psi\rangle$. Then we have that $\mathcal{T}^2|\psi\rangle = \mathcal{T}e^{i\phi}|\phi\rangle = e^{-i\phi}\mathcal{T}|\phi\rangle = e^{-i\phi}e^{i\phi}|\psi\rangle = |\psi\rangle$ and thus $\mathcal{T}^2 = +1$ which is a contradiction with the assumption that $\mathcal{T}^2 = -1$. □

Proposition. *Let $\mathcal{H}$ be a Hilbert space. Let $\mathcal{H}$ be a linear Hermitian operator with a non-empty point spectrum. Let $\mathcal{T} : \mathcal{H} \to \mathcal{H}$ be an anti-unitary bijection. If $\mathcal{T}^2 = -1$(fermion condition) and $[\mathcal{T}, \mathcal{H}] = 0$ ($\mathcal{T}$-invariance) then $\mathcal{H}$ has two orthogonal eigenvectors with the same eigenvalue.*

Proof. Since $\mathcal{H}$ has a non-empty point spectrum, there exists an eigenvector $|\psi\rangle$ with a real eigenvalue λ such that $\mathcal{H}|\psi\rangle = \lambda\psi$. Let $|\psi'\rangle = \mathcal{T}|\psi\rangle$. By $\mathcal{T}$-invariance, $\mathcal{H}|\psi'\rangle = \mathcal{T}\mathcal{H}|\psi\rangle = \lambda\mathcal{T}|\psi\rangle = \lambda|\psi'\rangle$ .The eigenvectors $|\psi\rangle$ and $|\psi'\rangle$ share the same eigenvalue λ. They are moreover orthogonal, since $\langle\psi|\psi'\rangle = \langle\psi|\mathcal{T}|\psi\rangle = \langle\psi|\mathcal{T}|\mathcal{T}^2|\psi\rangle^* = -\langle\psi|\mathcal{T}|\psi\rangle^* = -\langle\psi|\mathcal{T}|\psi\rangle = -\langle\psi'|\psi\rangle$ where the first equality follows from the fact that T is anti-unitary and the second from the fermion condition. □

Kramer's doublet

Applying the theorem of Kramer to the Bloch wave in an insulator, it holds that for any Bloch state $|\psi_{n,k}\rangle$, there is another state $|\phi_{n,k}\rangle$ which has the same energy.

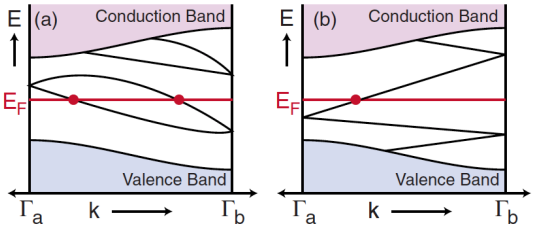

Figure B.1: Electronic dispersion between two boundary Kramer degenerate points $\Gamma_a = 0$ and $\Gamma_b = \pi/a$. Plot (a) shows the number of surface states crossing the Fermi energy E_F is even, whereas in plot (b) it is odd. An odd number of crossings leads to topologically protected metallic boundary states.[1]

Since each band intersecting E_F at k_x has a Kramer partner at $-k_x$, the bulk-boundary correspondence relates the number N_K of Kramer pairs of edge modes intersecting E_F to the change in the $\mathbb{Z}_2$ invariants across the interface, $N_K = \nu \mod 2$. There are several mathematical formulations of the $\mathbb{Z}_2$ invariant.

Appendix C

From the Dirac equation to the Weyl equation

The Dirac equation has been proposed by Paul Dirac as a particular incarnation of the Schrödinger equation, transforming it into a Lorentz covariant form, describing spin-1/2 free massive fermions. Starting from the Schrödinger equation of the form

$$i\hbar\frac{\partial}{\partial t}\psi = \left(\sum_{k=1,2,3}\frac{\hbar c}{i}\alpha^k\frac{\partial}{\partial x} + \beta mc^2\right)\psi$$

where α^k and β are some general $(n \times n)$-matrices and ψ is an n-vector, Dirac showed that one can satisfy

$$\left(i\hbar\frac{\partial}{\partial t}\right)^2\psi = \left(\sum_{k=1,2,3} -\hbar^2c^2\left(\frac{\partial}{\partial x}\right)^2 + m^2c^4\right)\psi$$

by choosing α^k and β as anti-commuting matrices that square to $\mathbb{1}$. For $n = 4$ $(3+1$ space-time dimensions) this yields the following matrices:

$$\alpha^i = \begin{pmatrix} 0 & \sigma^i \\ \sigma^i & 0 \end{pmatrix} \ , \ \beta = \begin{pmatrix} \mathbb{1}_{2\times2} & 0 \\ 0 & -\mathbb{1}_{2\times2} \end{pmatrix}.$$

Rewriting this in a more compact way yields the well-known γ-matrices (in the Dirac representation)

$$\gamma^0 = \beta = \begin{pmatrix} \mathbb{1}_{2\times 2} & 0 \\ 0 & -\mathbb{1}_{2\times 2} \end{pmatrix} \ , \ \gamma^i = \beta\alpha^i = \begin{pmatrix} 0 & \sigma^i \\ -\sigma^i & 0 \end{pmatrix}.$$

Using these matrices and the Einstein sum convention yields the Dirac equation:

$$\left(i\gamma^\mu \partial_\mu - \frac{mc}{\hbar}\right)\psi = 0.$$

Another possible representation for the γ-matrices is the chiral representation that is given by changing γ^0 to

$$\gamma^0_{ch} = \begin{pmatrix} 0 & \mathbb{1}_{2\times 2} \\ \mathbb{1}_{2\times 2} & 0 \end{pmatrix}$$

In this representation, the Dirac equation reads

$$\begin{pmatrix} -\frac{mc}{\hbar} & i(\partial_0 + \boldsymbol{\sigma}\cdot\boldsymbol{\nabla}) \\ i(\partial_0 - \boldsymbol{\sigma}\cdot\boldsymbol{\nabla}) & -\frac{mc}{\hbar} \end{pmatrix} \psi_{ch} = 0.$$

For free massless fermions, it holds that $m \to 0$. The Dirac equation then decouples into two independent sectors, namely the Weyl equations, as Weyl has shown in 1929 [71], given by:

$$i(\partial_0 - \boldsymbol{\sigma}\cdot\boldsymbol{\nabla})\psi_L = 0 \ \ , \ \ i(\partial_0 + \boldsymbol{\sigma}\cdot\boldsymbol{\nabla})\psi_R = 0.$$

Here $\psi_{R,L}$ represent two 2-spinors with definite opposite chirality. This shows that Weyl fermions, described by Weyl spinors, are particular massless Dirac fermions, namely independent ones with definite chirality.

Appendix D

Energy bands of model I and II

Model I, given by equation (M1) of section 6.1.1, respects time-reversal symmetry, and is defined on the cubic lattice. The non-interacting band structure is trivial and given by

$$\xi_n(\mathbf{k}) = \pm \left[4(\sin(k_x) - \sin(k_{x_0}))^2 + 4\sin^2(k_y) + 4(\sin(k_z) - \sin(k_{z_0}))^2\right]^{1/2}.$$

This yields 8 different solutions when setting $\xi_n(\mathbf{k})$ to zero, namely:

$$\begin{aligned}
\mathbf{K}_{WS_1} &= (k_{x_0}, 0, k_{z_0}) \\
\mathbf{K}_{WS_2} &= (\pi - k_{x_0}, 0, k_{z_0}) \\
\mathbf{K}_{WS_3} &= (k_{x_0}, 0, \pi - k_{z_0}) \\
\mathbf{K}_{WS_4} &= (\pi - k_{x_0}, 0, \pi - k_{z_0})
\end{aligned}$$

as well as

$$\begin{aligned}
\mathbf{K}_{WS_1'} &= (k_{x_0}, \pi, k_{z_0}) \\
\mathbf{K}_{WS_2'} &= (\pi - k_{x_0}, \pi, k_{z_0}) \\
\mathbf{K}_{WS_3'} &= (k_{x_0}, \pi, \pi - k_{z_0}) \\
\mathbf{K}_{WS_4'} &= (\pi - k_{x_0}, \pi, \pi - k_{z_0}).
\end{aligned}$$

Thus the Hamiltonian of model I preserves time-reversal symmetry, since $\Theta H(\mathbf{k})\Theta^{-1} = H(-\mathbf{k})$. However, the inversion symmetry $IH(\mathbf{k})I^{-1} = H(-\mathbf{k})$ is explicitly broken.

The tight-binding part of Model II was introduced in [63]. Below the non-interacting WSM band structure is presented. Diagonalizing the non-interacting Bloch Hamiltonian of equation (M2) of section 6.1.2 for $\epsilon_{\mathbf{k}} = 0$ and $t = 1$, the band structure yields the dispersion relation

$$\xi_n(\mathbf{k}) = \pm \left[(2(\cos(k_x) - \cos(k_0)) + m(2 - \cos(k_y) - \cos(k_z)))^2 + 4\sin^2(k_y) + 4\sin^2(k_z) \right]^{1/2}.$$

The non-interacting Weyl nodes are obtained from the zeros of $\zeta_n(k)$:

$$\begin{aligned}
\mathbf{k} &= (\pm k_0, 0, 0) \\
\mathbf{k} &= (\pm \cos^{-1}(\cos(k_0) - m), 0, \pi) \qquad \text{if } |\cos(k_0) - m| \leq 1 \\
\mathbf{k} &= (\pm \cos^{-1}(\cos(k_0) - m), \pi, 0) \qquad \text{if } |\cos(k_0) - m| \leq 1 \\
\mathbf{k} &= (\pm \cos^{-1}(\cos(k_0) - m), \pi, \pi) \qquad \text{if } |\cos(k_0) - 2m| \leq 1
\end{aligned}$$

When $m > 1$, the Hamiltonian has the minimal allowed number of Weyl nodes, i.e. only two. The Hamiltonian of model II breaks time-reversal symmetry, since $\Theta H \Theta^{-1} \neq H$, where $\Theta = e^{\frac{-i\pi\sigma_y}{h}} K$ where K is the complex conjugation operator as seen in Appendix B.

Appendix E

Analytical description of the dislocation modes in three-dimensions

Consider the effect of dislocations in the coarse-grained continuum theory obtained from the tight-binding model introduced in chapter 5. Such lattice defects are described within the elastic continuum theory using vielbeins, encoding the map from the perfect lattice to the distorted lattice. The torsion T^i and curvature R^i_j are related to the vielbeins E^i_α and the spin connection ω^i_j by the Einstein-Cartan structure equations

$$T^i = dE^i + \omega^i_j \wedge E^j$$

$$R^i_j = dw^i_j + \omega^i_k \wedge w^k_j$$

For a dislocation defect, the curvature vanishes while the torsion is singular, $T^i = b^i \delta(\mathbf{R})$ with $\mathbf{b}$ as the Burgers vector and $\mathbf{R}$ as the position of the dislocation line. Since the curvature tensor vanishes for a dislocation, the corresponding spin-connection can be set to zero.

E.1 Edge dislocations

In case of an edge dislocation oriented along the z-direction, the Vielbein takes the form

$$\hat{E} \equiv E^i_\alpha = \begin{pmatrix} 1 - \frac{by}{2\pi r^2} & \frac{bx}{2\pi r^2} & 0 \\ 0 & 1 & 0 \\ 0 & 0 & 1 \end{pmatrix}$$

where b is the magnitude of the Burgers vector b, which is assumed to be along the x-direction $\mathbf{b} = b\mathbf{e}_x$, and $r^2 \equiv x^2 + y^2$. The inverse of the above vielbein is readily found to be

$$\hat{E}^{-1} \equiv E^\alpha_i = \begin{pmatrix} \left(1 - \frac{by}{2\pi r^2}\right)^{-1} & -\frac{bx}{2\pi r^2}\left(1 - \frac{by}{2\pi r^2}\right)^{-1} & 0 \\ 0 & 1 & 0 \\ 0 & 0 & 1 \end{pmatrix}$$

Since for an elementary dislocation $b = a$ with a as the lattice constant, the distortion field $\mathbf{E}_i = \mathbf{e}_i + \boldsymbol{\varepsilon}_i$ to the leading order in a/r is then readily obtained

$$\boldsymbol{\varepsilon}_x = \frac{ay}{2\pi r^2}\mathbf{e}_x = \frac{y}{2\pi r^2}\mathbf{b}$$
$$\boldsymbol{\varepsilon}_y = \frac{ax}{2\pi r^2}\mathbf{e}_x = \frac{x}{2\pi r^2}\mathbf{b}$$

The corresponding gauge potential $\mathbf{A}_i = -\boldsymbol{\varepsilon}_i \cdot \mathbf{K}_{\text{inv}}$ with $\mathbf{K}_{\text{inv}}$ as the band-inversion momentum, can be then straightforwardly obtained

$$\mathbf{A} = \frac{-y\mathbf{e}_x + x\mathbf{e}_y}{2\pi r^2}(\mathbf{K}_{\text{inv}} \cdot \mathbf{b}) \equiv \frac{-y\mathbf{e}_x + x\mathbf{e}_y}{2\pi r^2}\boldsymbol{\Phi}$$

where $\boldsymbol{\Phi} = \mathbf{K}_{\text{inv}} \cdot \mathbf{b}$ represents and effective flux.

Appendix F

Calculation of the chiral anomaly

A generic low-energy model of two Weyl nodes of opposite chirality, separated in momentum space and in energy, is described by the momentum-space Hamiltonian

$$H = \tau_z \boldsymbol{\sigma} \cdot \mathbf{k} + \tau_z b_0 \sigma \cdot \mathbf{b}$$

where the Fermi velocity (in general different in different directions) is absorbed in the definition of momentum. The operator τ describes the node degree of freedom, while σ describes the conduction-valence band degree of freedom (non-degenerate conduction and valence bands touch at the Weyl nodes). Coupling the electrons to an external electromagnetic field, and representing the system in terms of the imaginary time action ($\tau = it$) yields [72]

$$S = \int d\tau d\mathbf{r}\ \psi^\dagger [\partial_\tau + ieA_0 + b_0\tau_z + \tau_z \sigma \cdot (-i\nabla + e\mathbf{A} + \mathbf{b}\tau_z)]\psi$$

where $A_\mu = (A_0, \mathbf{A})$ is the electromagnetic gauge potential and $\psi^\dagger, \psi$ are the Grassmann field variables[1] defined as $\psi(x) = \sum_n = \phi_n(x)c_n$ and $\psi^\dagger(x) = \sum_n \phi_n(x)^\dagger c_n^*$ are 4-component Grassmann spinors [66] that satisfy $\int d^4x \phi_n^*(x)\phi_m(x) = \delta_{nm}$ (in order to describe the Dirac field). The imaginary time action possesses a chiral symmetry

$$\psi \to e^{-i\tau_z\theta/2}\psi$$

which expresses an apparent separate conservation of the number of fermions of left and right chirality. Define the fieldθ as

$$\theta(\tau, \mathbf{r}) = 2\mathbf{b}\cdot\mathbf{r} - 2ib_0\tau.$$

Using this, the gauge transformation [72]

$$\psi \to e^{-i\tau_z\theta(\tau,\mathbf{r},)/2}\psi, \quad \psi^\dagger \to \psi^\dagger e^{i\tau_z\theta(\tau,\mathbf{r})/2}$$

eliminates the terms $\tau_z b_0$ and $\sigma\cdot\mathbf{b}$ from the imaginary time action. The imaginary time action then becomes

$$S = \int d\tau d\mathbf{r}\ \psi^\dagger[\partial_\tau + ieA_0 + \tau_z\sigma\cdot(-i\nabla + e\mathbf{A})]\psi$$

which describes two Weyl nodes of opposite chirality, existing at the same point in momentum space and in energy. This argument then leads one to the conclusion that the system of Weyl nodes, separated in energy and momentum, is equivalent to the system of two degenerate Weyl nodes and thus does not possess any special transport properties, which is incorrect [73]. The missing link in the above naive argument is precisely the chiral anomaly: while the imaginary time action does indeed possess the chiral symmetry, the gauge transformation changes not only the action itself, but also the measure of the path integral,

[1]The fields ψ and $\psi^\dagger$ are not complex conjugates of each other.

representing the partition function of the system

$$Z = \int D\psi^\dagger D\psi e^{-S[\psi^\dagger,\psi]}$$

where we assume that the electromagnetic field does not fluctuate, for simplicity. The change in the path integral measure, induced by the chiral gauge transformation gives rise precisely to an additional θ term in the action, obtained after Wick rotation to real time, as shown later on.

The Dirac γ-matrices are defined as

$$\gamma^0 = \tau^x, \gamma = i\tau^y\sigma, \gamma^5 = -i\gamma^0\gamma^1\gamma^2\gamma^3 = \tau^z.$$

Further defining $\gamma^4 = -i\gamma^0$, we can rewrite the imaginary time action into the relativistic action as

$$S = \int d^4x\ \bar{\psi}\ i\ \gamma^\mu(\partial_\mu + ieA_\mu + ib_\mu\gamma^5)\psi$$

where $\mu = 1, \ldots, 4$, $\bar{\psi} = \psi^\dagger\gamma^0$, $b_4 = -ib_0$ and $\int d^4x$ denotes the integral over the four-dimensional Euclidean space-time. To eliminate the b_μ term from the equation above, define the following sequence of infinitesimal gauge transformations [72]

$$\psi \to e^{-ids\theta(x)\gamma^5/2}\psi \quad , \quad \bar{\psi} \to \bar{\psi}e^{-ids\theta(x)\gamma^5/2}$$

where $\theta(x) = 2b_\mu x^\mu$ and the sign of the exponential in the second line above follows from the fact that γ^5 anti-commutes with γ^0. The variable $s \in [0, 1]$, whose differential ds appears in the infinitesimal gauge transformation above, parametrizes the infinite sequence of the chiral gauge transformations.

We need to find how the infinitesimal transformation changes the path integral measure $D\bar{\psi}D\psi$.

Consider the $3+1$ dimensional Dirac operator, taken at stage s of the sequence of infinitesimal chiral transformation [72]

$$\not{D} = \gamma^\mu[\partial_\mu + ieA_\mu + ib_\mu(1-s)\gamma^5].$$

Since γ^μ are anti-Hermitian, $\not{D}$ is a Hermitian operator [73]. Assuming that $\not{D}\phi_n(x) = \epsilon_n\phi_n(x)$ where ϵ_n are real eigenvalues and ϕ_n our 4 -component spinor eigenfunctions such that $\int d^4x\phi_n^*(x)\phi_m(x) = \delta_{nm}$. Given a complete set of eigenfunctions $\phi_n(x)$, this forms a basis and thus we can write:

$$\psi(x) = \sum_n \phi_n(x)c_n, \quad \bar{\psi}_n(x) = \sum_n \phi_n(x)\bar{c_n}$$

where c_n and $\bar{c}_n$ represent the new Grassmann variables. Subsequently we get:

$$\begin{aligned}\psi'(x) &= e^{-ids\theta(x)\gamma^5/2}\phi(x) \\ &\underset{\text{Series exp.}}{=} [1 - ids\theta(x)\gamma^5/2]\sum_n \phi_n(x)c_n = \sum_n \phi_n(x)c'_n\end{aligned}$$

$$\begin{aligned}\bar{\psi}'(x) &= \bar{\phi}'(x)e^{-ids\theta(x)\gamma^5/2} \\ &\underset{\text{Series exp.}}{=} \sum_n \phi_n^*(x)\bar{c}_n[1 - ids\theta(x)\gamma^5/2] = \sum_n \phi_n^*(x)\bar{c}'_n\end{aligned}$$

Define the infinitesimal chiral transformation operator as

$$U_{nm} = \delta_{nm} - ds\frac{i}{2}\int d^4x\ \phi_n^*(x)\theta(x)\gamma^5\phi_m(x)$$

then we get

$$c'_n = \sum_m U_{nm}c_m, \quad \bar{c}'_m = \sum_n U_{mn}\bar{c}_n.$$

This gives the following integral Jacobian, corresponding to the chiral gauge transformation

$$J = \det(U^{-2}) = e^{\ln(\det(U^{-2}))} = e^{-2\,\mathrm{tr}[\ln(U)]} = e^{ids\int d^4x\ \sum_n \phi_n^*(x)\theta(x)\gamma^5\phi_n(x)}.$$

Consider

$$I(x) = \sum_n \phi_n^*(x)\gamma^5\phi_n(x).$$

Note that γ^5 anti-commutes with $\not{D}$ and thus only zero eigenmodes contribute to $\int d^4x I(x)$. Therefore we get

$$\int d^4x I(x) = n_+ - n_- = \mathrm{Ind}(\not{D})$$

where $n_\pm$ is the number of zero-mode eigenstates with positive (negative) chirality. We can write $I(x)$ as follows:

$$I(x) = \lim_{M\to\infty} \sum_n \phi_n^*(x) e^{-\epsilon_n^2/M^2}\gamma^5\phi_n(x) = \lim_{M\to\infty} \sum_n \phi_n^*(x) e^{-\not{D}^2/M^2}\gamma^5\phi_n(x).$$

Squaring the Dirac operator yields:

$$\not{D}^2 = -D_\mu D^\mu - (1-s)^2 b_\mu b^\mu + \frac{ie}{4}[\gamma^\mu,\gamma^\nu]F_{\mu\nu} + i(1-s)[\gamma^\mu,\gamma^\nu]b_\mu D_\nu\gamma^5$$

where $D_\mu = \partial_\mu + ieA_\mu$ and we made use of

$$[D_\mu, D_\nu] = ie(\partial_\mu A_\nu - \partial_\nu A_\mu) = ieF_{\mu\nu}$$

This yields the completeness relation $\sum_n \phi_n^*(x)\phi_n(y) = \delta(x-y)$. Using these relations we get for $I(x)$

$$\begin{aligned} I(x) &= \lim_{M\to\infty} \int \frac{d^4k}{(2\pi)^4} \operatorname{tr}\gamma^5 e^{-ikx} e^{-\not{D}^2/M^2} e^{ikx} \\ &= \lim_{M\to\infty} \int \frac{d^4k}{(2\pi)^4} \operatorname{tr}\gamma^5 \exp\left[\frac{(ik_\mu + D_\mu)^2}{M^2} + \frac{(1-s)^2 b_\mu b^\mu}{M^2}\right. \\ &\quad \left. -\frac{ie}{4M^2}[\gamma^\mu,\gamma^\nu]F_{\mu\nu} - \frac{i(1-s)}{M^2}[\gamma^\mu,\gamma^\nu]b_\mu(ik_\nu + D_\nu)\gamma^5\right] \end{aligned}$$

Rescaling the momentum integration variable $k_\mu \to Mk_\mu$ and leaving only terms that survive in the limit $M\to\infty$ we get:

$$I(x) = -\frac{e^2}{32}\operatorname{tr}\gamma^5[\gamma^\mu,\gamma^\nu][\gamma^\alpha,\gamma^\beta]F_{\mu\nu}F_{\alpha\beta} = \frac{e^2}{32\pi^2}\epsilon^{\mu\nu\alpha\beta}F_{\mu\nu}F_{\alpha\beta}$$

Going back to the Jacobian we obtain

$$J = e^{-ids \int d^4x \theta(x) I(x)}$$

yielding

$$\begin{aligned} S_\theta &= i \int_0^1 ds \int d^4x \; \theta(x) I(x) = \frac{ie^2}{32\pi^2} \int d^4x \; \theta(x) \epsilon^{\mu\nu\alpha\beta} F_{\mu\nu} F_{\alpha\beta} \\ &\overset{\tau \to it}{=} \frac{e^2}{32\pi^2} \int dt d\mathbf{r} \; \theta(x) \epsilon^{\mu\nu\alpha\beta} F_{\mu\nu} F_{\alpha\beta} \end{aligned}$$

Therefore the topological response of Weyl semimetals is described by an axion-type action with the axion field θ. Thus we see that the Weyl nodes separated in momentum space and in energy give rise to an induced θ axion field in the action of the electromagnetic field.

Appendix G

Total current in the presence of dislocations

For a system that exhibits translational symmetry in a certain direction, the total current is always zero, even in the presence of a magnetic field or lattice stain and dislocations. The argument is the extension of that presented in Ref.[60]. Recall the action from Appendix 3.4, where

$$S = \int d\tau d\mathbf{r}\ \psi^\dagger[\partial_\tau + ieA_0 + b_0\tau_z + \tau_z\sigma\cdot(-i\nabla + e\mathbf{A} + \mathbf{b}\tau_z)\psi$$

which in a more compact form (using the Einstein summation convention) yields

$$S = \int dx^\mu\ \psi^\dagger[\tau_z\sigma^\mu\cdot(-i\nabla_\mu + e\mathbf{A}_\mu + \mathbf{b}_\mu\tau_z)]\psi.$$

Adding a dislocation results in an additional potential term $V_\mu = V(x^\mu)$. This results in

$$S = \int dx^\mu\ \psi^\dagger[\tau_z\sigma^\mu\cdot(-i\nabla_\mu + e\mathbf{A}_\mu + \mathbf{b}_\mu\tau_z) + V_\mu]\psi = \int dx^\mu\psi^\dagger H(x_\mu)\psi.$$

Imposing periodicity in the z-direction implies $A(x^\mu) = A(x'^\mu)$ and $V(x^\mu) = V(x'^\mu)$ where $x'^\mu = (\tau, x, y, z + a)$.

For comfort, we define $\rho = (\tau, x, y)$ so that $x^\mu = (\rho, z)$. Define the Bloch wave function $\psi_{n,k_z}(\rho, z) = e^{ik_z z} u_{n,k_z}(\rho, z)$ with eigenenergy ϵ_{n,k_z}.
The total current along the z-direction is then given by

$$\begin{aligned} J_z &= \sum_n \int_{BZ} \frac{dk_z}{2\pi} \int dx^\mu \psi^\dagger_{n,k_z}(\rho, z) \frac{\partial H}{\partial A_z} \psi_{n,kz}(\rho, z) n_F(\epsilon_{n,k_z}) \\ &= -\sum_n \int_{BZ} \frac{dk_z}{2\pi} \int dx^\mu u^*_{n,k_z}(\rho, z) \frac{\partial H_{k_z}}{\partial k_z} u_{n,kz}(\rho, z) n_F(\epsilon_{n,k_z}) \end{aligned}$$

where $H_{k_z} = e^{-ik_z z} H e^{ik_z z}$. Using the fact that $\int dx^\mu u^*_{n,k_z} u_{n,k_z} = 1$ and thus $frac\partial\partial k_z \int dx^\mu u^*_{n,k_z} u_{n,k_z} = 0$ this yields

$$\begin{aligned} J_z &= -\sum_n \int_{BZ} \frac{dk_z}{2\pi} \frac{\partial}{\partial k_z} \int dx^\mu u^*_{n,k_z}(\rho, z) h_{k_z} u_{n,kz}(\rho, z) n_F(\epsilon_{n,k_z}) \\ &= -\sum_n \int_{BZ} \frac{dk_z}{2\pi} \frac{\partial}{\partial k_z} \int dx^\mu u^*_{n,k_z}(\rho, z) \epsilon_{n,k_z} u_{n,kz}(\rho, z) n_F(\epsilon_{n,k_z}) \\ &= \sum_n \int_{BZ} \frac{dk_z}{2\pi} \frac{\partial \epsilon_{n,k_z}}{\partial k_z} \int dx^\mu u^*_{n,k_z}(\rho, z) u_{n,kz}(\rho, z) n_F(\epsilon_{n,k_z}) \\ &= \sum_n \int_{BZ} \frac{dk_z}{2\pi} \frac{\partial \epsilon_{n,k_z}}{\partial k_z} n_F(\epsilon_{n,k_z}) \\ &= -\frac{1}{2\pi} \sum_n \sum_{i=1,\ldots,i_n} \int_{\epsilon_{n,k_{i-1}}}^{\epsilon_{n,k_i}} d\epsilon \; n_F(\epsilon) \end{aligned}$$

It holds that for each region $k \in (k_{i-1}, k)$ that $\epsilon_{n,k}$ increases or decreases monotonically and due to the periodicity it holds that $\epsilon_{n,k_0} = \epsilon_{n,k_{\frac{\pi}{a}}}$. This results into $J_z = 0$. Therefore, the total current in a direction in which the system possesses translational symmetry is equal to zero. This comes from the fact that the integral over space-time of $|e_{n,k_z}(\rho, z)|$ equal 1.

Bibliography

[1] M. Z. Hasan and C. L. Kane, "Colloquium: Topological insulators," *Reviews of Modern Physics*, vol. 82, pp. 3045–3067, nov 2010.

[2] M. Averett, "Topology," April 2011.

[3] D. Allegretti, "Notes on Topological Quantum Field Theory."

[4] K. Klitzing, G. Dorda, and M. Pepper, "New Method for High-Accuracy Determination of the Fine-Structure Constant Based on Quantized Hall Resistance," *Physical Review Letters*, vol. 45, pp. 494–497, aug 1980.

[5] T. Ando, "Theory of Quantum Transport in a Two-Dimensional Electron System under Magnetic Fields. III. Many-Site Approximation," *Journal of the Physical Society of Japan*, vol. 37, pp. 622–630, sep 1974.

[6] Y. Ando and L. Fu, "Topological Crystalline Insulators and Topological Superconductors: From Concepts to Materials," *Annual Review of Condensed Matter Physics*, vol. 6, pp. 361–381, mar 2015.

[7] A. Altland and M. R. Zirnbauer, "Nonstandard symmetry classes in mesoscopic normal-superconducting hybrid structures," *Physical Review B*, vol. 55, pp. 1142–1161, jan 1997.

[8] D. Bulmash, P. Hosur, S.-C. Zhang, and X.-L. Qi, "Unified Topological Response Theory For Gapped and Gapless Free Fermions," *Physical Review X*, vol. 5, p. 021018, may 2015.

[9] G. Y. Cho and J. E. Moore, "Topological BF field theory description of topological insulators," *Annals of Physics*, vol. 326, pp. 1515–1535, jun 2011.

[10] C. L. Kane and E. J. Mele, "Z_{2} Topological Order and the Quantum Spin Hall Effect," *Physical Review Letters*, vol. 95, p. 146802, sep 2005.

[11] L. Fu and C. L. Kane, "Time reversal polarization and a Z 2 adiabatic spin pump," *Physical Review B*, vol. 74, p. 195312, nov 2006.

[12] J. Moore, "Topological insulators: The next generation," *Nature Physics*, vol. 5, pp. 378–380, jun 2009.

[13] X.-L. Qi, Y.-S. Wu, and S.-C. Zhang, "General theorem relating the bulk topological number to edge states in two-dimensional insulators," *Physical Review B*, vol. 74, p. 045125, jul 2006.

[14] J. E. Moore, "The birth of topological insulators.," *Nature*, vol. 464, no. 7286, pp. 194–198, 2010.

[15] A. Altland and D. Bagrets, "Theory of the strongly disordered Weyl semimetal," *Physical Review B*, vol. 93, p. 075113, feb 2016.

[16] X. Wan, A. M. Turner, A. Vishwanath, and S. Y. Savrasov, "Topological semimetal and Fermi-arc surface states in the electronic structure of pyrochlore iridates," *Physical Review B - Condensed Matter and Materials Physics*, vol. 83, no. 20, pp. 1–9, 2011.

[17] F. D. M. Haldane, "Attachment of Surface "Fermi Arcs" to the Bulk Fermi Surface: "Fermi-Level Plumbing" in Topological Metals," vol. 0708, no. 3, p. 5, 2014.

[18] L. Balents, "Viewpoint: Weyl electrons kiss," *Physics*, vol. 4, may 2011.

[19] S.-M. Huang, S.-Y. Xu, I. Belopolski, C.-C. Lee, G. Chang, B. Wang, N. Alidoust, G. Bian, M. Neupane, C. Zhang, S. Jia, A. Bansil, H. Lin, and M. Z. Hasan, "A Weyl Fermion semimetal with surface Fermi arcs in the transition metal monopnictide TaAs class.," *Nature communications*, vol. 6, p. 7373, jan 2015.

[20] A. A. Zyuzin, S. Wu, and A. A. Burkov, "Weyl semimetal with broken time reversal and inversion symmetries," *Physical Review B*, vol. 85, p. 165110, apr 2012.

[21] M. Kargarian, M. Randeria, and Y.-M. Lu, "Are the double Fermi arcs of Dirac semimetals topologically protected?," p. 10, sep 2015.

[22] S. Murakami, "Phase transition between the quantum spin Hall and insulator phases in 3D: emergence of a topological gapless phase," *New Journal of Physics*, vol. 9, pp. 356–356, sep 2007.

[23] J. Xiong, S. K. Kushwaha, T. Liang, J. W. Krizan, W. Wang, R. J. Cava, and N. P. Ong, "Signature of the chiral anomaly in a Dirac semimetal: a current plume steered by a magnetic field," p. 8, mar 2015.

[24] T. Meng, *Quantum Critical Matter: Quantum Phase Transitions with Multiple Dynamics and Weyl Superconductors*. PhD thesis, Universität zu Köln, 2012.

[25] S.-Y. Xu, I. Belopolski, D. S. Sanchez, C. Zhang, G. Chang, C. Guo, G. Bian, Z. Yuan, H. Lu, T.-R. Chang, P. P. Shibayev, M. L. Prokopovych, N. Alidoust, H. Zheng, C.-C. Lee, S.-M. Huang, R. Sankar, F. Chou, C.-H. Hsu, H.-T. Jeng, A. Bansil, T. Neupert, V. N. Strocov, H. Lin, S. Jia, and M. Z. Hasan, "Experimental discovery of a topological weyl semimetal state in tap," *Science Advances*, vol. 1, no. 10, 2015.

[26] A. A. Soluyanov, D. Gresch, Z. Wang, Q. Wu, M. Troyer, X. Dai, and B. A. Bernevig, "Type-II Weyl semimetals.," *Nature*, vol. 527, pp. 495–8, nov 2015.

[27] H. Omid, "Chern-Simons terms in the 3D Weyl semi-metals," may 2014.

[28] B. A. Bernevig, "It's been a Weyl coming," *Nat Phys*, vol. 11, pp. 698–699, sep 2015.

[29] A. M. Turner and A. Vishwanath, "Beyond Band Insulators: Topology of Semi-metals and Interacting Phases," jan 2013.

[30] J. Zwanziger, M. Koenig, and A. Pines, "Berry's phase," *Annual Review of Physical Chemistry*, vol. 41, no. 1, pp. 601–646, 1990.

[31] A. Messiah, *Quantum Mechanics*. Dover books on physics, Dover Publications, 1961.

[32] M. V. Berry, "Quantal Phase Factors Accompanying Adiabatic Changes," *Proceedings of the Royal Society A: Mathematical, Physical and Engineering Sciences*, vol. 392, pp. 45–57, mar 1984.

[33] X. Huang, L. Zhao, Y. Long, P. Wang, D. Chen, Z. Yang, H. Liang, M. Xue, H. Weng, Z. Fang, X. Dai, and G. Chen, "Observation of the Chiral-Anomaly-Induced Negative Magnetoresistance in 3D

Weyl Semimetal TaAs," *Physical Review X*, vol. 5, p. 031023, aug 2015.

[34] L. Lu, Z. Wang, D. Ye, L. Ran, L. Fu, J. D. Joannopoulos, and M. Soljai, "Experimental observation of weyl points," *Science*, 2015.

[35] F. D. M. Haldane, "Berry curvature on the fermi surface: Anomalous hall effect as a topological fermi-liquid property," *Physical Review Letters*, vol. 93, no. 20, pp. 1–4, 2004.

[36] H. Nielsen and M. Ninomiya, "Absence of neutrinos on a lattice: (i). proof by homotopy theory," *Nuclear Physics B*, vol. 185, no. 1, pp. 20 – 40, 1981.

[37] H. Nielsen and M. Ninomiya, "Absence of neutrinos on a lattice: (ii). intuitive topological proof," *Nuclear Physics B*, vol. 193, no. 1, pp. 173 – 194, 1981.

[38] H. Nielsen and M. Ninomiya, "A no-go theorem for regularizing chiral fermions," *Physics Letters B*, vol. 105, pp. 219–223, oct 1981.

[39] H. Nielsen and M. Ninomiya, "The Adler-Bell-Jackiw anomaly and Weyl fermions in a crystal," *Physics Letters B*, vol. 130, pp. 389–396, nov 1983.

[40] T. Morimoto and A. Furusaki, "Weyl and Dirac semimetals with Z 2 topological charge," *Physical Review B*, vol. 89, p. 235127, jun 2014.

[41] J. Behrends, A. G. Grushin, T. Ojanen, and J. H. Bardarson, "Visualizing the chiral anomaly in Dirac and Weyl semimetals with photoemission spectroscopy," p. 4, mar 2015.

[42] S. L. Adler, "Axial-Vector Vertex in Spinor Electrodynamics," *Physical Review*, vol. 177, pp. 2426–2438, jan 1969.

[43] J. S. Bell and R. Jackiw, "A PCAC puzzle: $\pi 0 \gamma \gamma$ in the σ-model," *Il Nuovo Cimento A*, vol. 60, pp. 47–61, mar 1969.

[44] J. Xiong, S. K. Kushwaha, T. Liang, J. W. Krizan, M. Hirschberger, W. Wang, R. J. Cava, and N. P. Ong, "Evidence for the chiral anomaly in the Dirac semimetal Na3Bi.," *Science (New York, N.Y.)*, vol. 350, pp. 413–416, sep 2015.

[45] A. A. Burkov, "Chiral anomaly without relativity.," *Science (New York, N.Y.)*, vol. 350, pp. 378–9, oct 2015.

[46] D.-F. Xu, Y.-P. Du, Z. Wang, Y.-P. Li, X.-H. Niu, Q. Yao, D. Pavel, Z.-A. Xu, X.-G. Wan, and D.-L. Feng, "Observation of Fermi Arcs in Non-Centrosymmetric Weyl Semi-Metal Candidate NbP," *Chinese Physics Letters*, vol. 32, p. 107101, oct 2015.

[47] T. Bzdušek, A. Rüegg, and M. Sigrist, "Weyl semimetal from spontaneous inversion symmetry breaking in pyrochlore oxides," *Physical Review B*, vol. 91, p. 165105, apr 2015.

[48] V. Aji, "Adler-Bell-Jackiw anomaly in Weyl semimetals: Application to pyrochlore iridates," *Physical Review B*, vol. 85, p. 241101, jun 2012.

[49] H. Yamada and S. Takada, "Negative Magnetoresistance of Ferromagnetic Metals due to Spin Fluctuations," *Progress of Theoretical Physics*, vol. 48, pp. 1828–1848, dec 1972.

[50] Y. Ran, Y. Zhang, and A. Vishwanath, "One-dimensional topologically protected modes in topological insulators with lattice dislocations," *Nature Physics*, vol. 5, pp. 298–303, mar 2009.

[51] D. Vollhardt and P. Woelfle, "Superfluid Helium 3: Link between Condensed Matter Physics and Particle Physics," p. 11, dec 2000.

[52] M. Postma and B. Hartmann, "Zero modes on cosmic string loops," p. 27, jun 2007.

[53] V. Volterra, "Sur l'quilibre des corps lastiques multiplement connexes," *Annales scientifiques de l'cole Normale Suprieure*, vol. 24, pp. 401–517, 1907.

[54] R.-J. Slager, *The symmetry of crystals and the topology of electrons*. PhD thesis, Leiden University, 2015.

[55] R.-J. Slager, A. Mesaros, V. Juričić, and J. Zaanen, "Interplay between electronic topology and crystal symmetry: Dislocation-line modes in topological band insulators," *Physical Review B*, vol. 90, p. 241403, dec 2014.

[56] A. G. Grushin, "Consequences of a condensed matter realization of Lorentz-violating QED in Weyl semi-metals," *Physical Review D*, vol. 86, p. 045001, aug 2012.

[57] D. T. Son and N. Yamamoto, "Berry curvature, triangle anomalies, and the chiral magnetic effect in Fermi liquids.," *Physical review letters*, vol. 109, p. 181602, nov 2012.

[58] P. Goswami and S. Tewari, "Axionic field theory of (3 + 1) -dimensional Weyl semimetals," *Physical Review B*, vol. 88, p. 245107, dec 2013.

[59] J. S. Bell and R. W. Jackiw, "A pcac puzzle," *Nuovo Cimento*, vol. 60, no. CERN-TH-920, pp. 47–61, 1969.

[60] M. M. Vazifeh and M. Franz, "Electromagnetic response of Weyl semimetals.," *Physical review letters*, vol. 111, p. 027201, jul 2013.

[61] P. Hosur and X. Qi, "Recent developments in transport phenomena in Weyl semimetals," *Comptes Rendus Physique*, vol. 14, pp. 857–870, nov 2013.

[62] W. Witczak-Krempa, M. Knap, and D. Abanin, "Interacting Weyl semimetals: characterization via the topological Hamiltonian and its breakdown.," *Physical review letters*, vol. 113, p. 136402, sep 2014.

[63] K.-Y. Yang, Y.-M. Lu, and Y. Ran, "Quantum Hall effects in a Weyl semimetal: Possible application in pyrochlore iridates," *Physical Review B*, vol. 84, p. 075129, aug 2011.

[64] S. M. Young, S. Zaheer, J. C. Y. Teo, C. L. Kane, E. J. Mele, and A. M. Rappe, "Dirac Semimetal in Three Dimensions," *Physical Review Letters*, vol. 108, p. 140405, apr 2012.

[65] H. Sumiyoshi and S. Fujimoto, "Torsional chiral magnetic effect in Weyl semimetal with topological defect," p. 10, sep 2015.

[66] M. Peskin and D. Schroeder, *An Introduction to Quantum Field Theory*. Advanced book classics, Addison-Wesley Publishing Company, 1995.

[67] A. A. Burkov, "Chiral anomaly and transport in Weyl metals.," *Journal of physics. Condensed matter : an Institute of Physics journal*, vol. 27, p. 113201, mar 2015.

[68] R.-J. Slager, "Topological aspects of Aharonov-Bohm vortices in topological band insulators," Master's thesis, Leiden University, the Netherlands, 2010.

[69] M. Gyry, "A new proof of Wigner's theorem," *Reports on Mathematical Physics*, vol. 54, pp. 159–167, oct 2004.

[70] R. Simon, N. Mukunda, S. Chaturvedi, and V. Srinivasan, "Two elementary proofs of the Wigner theorem on symmetry in quantum mechanics," *Physics Letters A*, vol. 372, pp. 6847–6852, nov 2008.

[71] H. Weyl, "GRAVITATION AND THE ELECTRON.," *Proceedings of the National Academy of Sciences of the United States of America*, vol. 15, pp. 323–34, apr 1929.

[72] A. A. Zyuzin and A. A. Burkov, "Topological response in Weyl semimetals and the chiral anomaly," *Physical Review B*, vol. 86, p. 115133, sep 2012.

[73] A. A. Burkov, "Chiral anomaly and transport in Weyl metals.," *Journal of physics. Condensed matter : an Institute of Physics journal*, vol. 27, p. 113201, mar 2015.